Mon. Not. R. Astron. Soc. **000**, 1–**??** (2015) Printed 3 March 2022 (MN LATEX style file v2.2)

Cosmic Neutron Star Merger Rate and Gravitational Waves constrained by the R Process Nucleosynthesis

Elisabeth Vangioni[1⋆], Stéphane Goriely[2], Frédéric Daigne[1], Patrick François[3], and Krzysztof Belczynski[4]

[1]*Sorbonne Universités, UPMC Univ Paris 6 et CNRS, UMR 7095, Institut d'Astrophysique de Paris, 98 bis bd Arago, 75014 Paris, France*
[2]*Institut d'Astronomie et d'Astrophysique, CP 226, Université Libre de Bruxelles, 1050 Brussels, Belgium*
[3]*GEPI, Paris-Meudon Observatory, 61 Avenue de l'Observatoire, F-75014 Paris, France*
[4]*Astronomical Observatory, University of Warsaw, Al. Ujazdowskie 4, 00-478 Warsaw, Poland*

arXiv:1501.01115v2 [astro-ph.HE] 2 Oct 2015

3 March 2022

ABSTRACT

The cosmic evolution of the neutron star merger (NSM) rate can be deduced from the observed cosmic star formation rate. This allows to estimate the rate expected in the horizon of the gravitational wave detectors advanced Virgo and ad LIGO and to compare those rates with independent predictions. In this context, the rapid neutron-capture process, or r-process, can be used as a constraint assuming NSM is the main astrophysical site for this nucleosynthetic process. We compute the early cosmic evolution of a typical r-process element, Europium. Eu yields from NSM are taken from recent nucleosynthesis calculations. The same approach allows to compute the cosmic rate of Core Collapse SuperNovae (CCSN) and the associated evolution of Eu.

We find that the bulk of Eu observations at [Fe/H] > -2.5 can be rather well fitted by either CCSN or NSM scenarios. However, at lower metallicity, the early Eu cosmic evolution favors NSM as the main astrophysical site for the r-process. A comparison between our calculations and spectroscopic observations at very low metallicities allows us to constrain the coalescence timescale in the NSM scenario to $\sim$ 0.1–0.2 Gyr. These values are in agreement with the coalescence timescales of some observed binary pulsars. Finally, the cosmic evolution of Eu is used to put constraints on i) the NSM rate, ii) the merger rate in the horizon of the gravitational wave detectors advanced Virgo/ad LIGO, as well as iii) the expected rate of electromagnetic counterparts to mergers ("kilonovae") in large near-infrared surveys.

Key words: Cosmology: dark ages, first stars, Physical Data and Processes: gravitational waves, nucleosynthesis, Stars: supernovae, neutron stars.

1 INTRODUCTION

Recently, a special attention has been paid to neutron star (NS)–NS or NS–black hole (BH) mergers (hereafter NSM), considered today as the most promising sources of gravitational waves for ground-based detectors such as advanced Virgo/ad Ligo (Phinney 1991; Narayan et al. 1991; Virgo collaboration 2009; Abadie et al. 2010; LIGO Scientific collaboration 2011; Aasi et al. 2014a,b,c; Belczynski et al. 2014) but also because several evidences (see Berger 2014, for a recent review) suggest in addition that these events are the progenitors of short gamma-ray bursts (GRB) (Paczynski 1986; Eichler et al. 1989; Narayan et al. 1992; Mochkovitch et al. 1993). Recent simulations show that, after the merger, the relic BH-torus system can produce an ultra-relativistic ejection along its rotation axis (Rezzolla et al. 2011), potentially leading to a short GRB. The similarities between the properties of the prompt emission in short and long GRBs (se e.g. Guiriec et al. 2010) suggest that the same dissipation process is at work in these two classes of bursts (Bošnjak & Daigne 2014) and that the main differences are the lifetime of the central engine, leading in the case of binary compact objects to shorter events, and the density of the circumburst medium, leading to weaker afterglows (Nakar 2007). In addition, hydrodynamic simulations have confirmed that a non-negligible amount of matter, typically about 10^{-3} to 10^{-2} $M_\odot$, can be ejected quasi-isotropically (Janka et al. 1999; Rosswog et al. 1999, 2004; Oechslin et al. 2007; Goriely et al. 2011; Bauswein et al. 2013; Goriely et al. 2013; Just et al. 2015; Wanajo et al. 2014) and that the matter ejected in such NSM events is essentially made of r-process nuclei, shedding a new light on a old mystery.

The r-process, or the rapid neutron-capture process, of stellar nucleosynthesis is invoked to explain the production of the stable (and some long-lived radioactive) neutron-rich nuclides heavier than iron that are observed in stars of various metallicities, as

⋆ e-mail:vangioni@iap.fr

© 2015 RAS

well as in the solar system (for a review, see Arnould et al. 2007). The r-process remains the most complex nucleosynthetic process to model from the astrophysics as well as nuclear-physics points of view. The site(s) of the r-process is (are) not identified yet, all the proposed scenarios facing serious problems. Complex—and often exotic—sites have been considered in the hope of identifying astrophysical conditions in which the production of neutrons is large enough to give rise to a successful r-process.

Progress in the modelling of type-II supernovae and long GRBs has raised a lot of excitement about the so-called neutrino-driven wind environment. However, until now a successful r-process cannot be obtained *ab initio* without tuning the relevant parameters (neutron excess, entropy, expansion timescale) in a way that is not supported by the most sophisticated existing models (Wanajo et al. 2011; Janka 2012).

Early in the development of the theory of nucleosynthesis, an alternative to the r-process in high-temperature supernova environments was proposed (Tsuruta & Cameron 1965). It relies on the fact that at high densities (typically $\rho > 10^{10}$ g/cm^3) matter tends to be composed of nuclei lying on the neutron-rich side of the valley of nuclear stability as a result of free-electron captures. The astrophysical plausibility of this scenario in accounting for the production of the r-nuclides has long been questioned. It remained largely unexplored until the study of the decompression of cold neutronised matter resulting from tidal effects of a BH on a NS companion (Lattimer & Schramm 1974; Lattimer et al. 1977; Meyer 1989). Many investigations with growing sophistication have now confirmed NSM ejecta as viable sites for strong r-processing (Arnould et al. 2007; Goriely et al. 2011; Bauswein et al. 2013; Goriely et al. 2013; Just et al. 2015; Freiburghaus et al. 1999; Goriely et al. 2005; Metzger et al. 2010; Roberts et al. 2011; Korobkin et al. 2012; Wanajo et al. 2014). In particular, recent nucleosynthesis calculations (Just et al. 2015) show that the combined contributions of both the dynamical (prompt) ejecta expelled during the binary NS-NS or NS-BH merger and the neutrino and viscously driven outflows generated during the post-merger remnant evolution of the relic BH-torus systems lead to the production of r-process elements from $A \gtrsim 90$ up to thorium and uranium with an abundance distribution that reproduce extremely well the solar distribution, as well as the elemental distribution spectroscopically determined in very-low-metallicity stars. The ejected mass of r-process material, combined with the predicted astrophysical event rate (around 10^{-5} yr^{-1} in the Milky Way (Dominik et al. 2012) can account for the majority of r-material in our Galaxy (Goriely et al. 2011; Bauswein et al. 2013; Just et al. 2015).

In NSM, nearly all of the ejecta are converted to r-process nuclei, whose radioactive decay heating leads to potentially observable electromagnetic radiation in the optical and infrared bands (Li & Paczyński 1998; Metzger et al. 2010) with 100–1000 times fainter peak brightnesses than those of typical supernovae and durations of only days (Goriely et al. 2011; Roberts et al. 2011; Bauswein et al. 2013). These "macronovae" or "kilonovae" are intensely searched for (with a recent, possible first success in association with the short GRB 130603B, see Berger et al. 2013; Tanvir et al. 2013). Their unambiguous discovery would constitute the first detection of r-material in situ.

In the present paper, our primary goal is to predict the cosmic evolution of the NSM that can be deduced from the observed history of the star formation rate (SFR), including the recent constraints obtained at high redshift (Behroozi et al. 2013; Behroozi & Silk 2015; Oesch et al. 2014; Bouwens et al 2014; Kistler et al. 2013; Trenti et al. 2013). Computing the NSM rate requires to determine poorly known parameters, namely the fraction of NS in a binary system with another NS or a BH, and the characteristic coalescence timescale of such a system. To constrain these parameters, we model the associated evolution of a typical r-process element, Europium, by assuming NSM as the main astrophysical site of the r-process and adopting the most recent nucleosynthetic calculations (Goriely et al. 2011; Bauswein et al. 2013; Just et al. 2015), and we compare to the available observations in old stars of the Galactic halo and in external galaxies. Once the merger rate has been determined, it is possible to estimate the expected event rate for the new generation of gravitational wave detectors (advanced Virgo and LIGO), as well as the expected detection rate of kilonovae in present and future optical/near-infrared large surveys. The same approach can be followed to determine, without any new parameter, the CCSN rate, hence the predicted evolution of Europium in the alternative scenario where r-process elements are produced mainly in such stellar explosions.

The paper is organized as follows: in Sect. 2, we select three possible scenarios for the SFR, which are representative of the current uncertainties at high redshift, and we describe how the CCSN and NSM rates can be deduced from the SFR, both scenarios still depending on given unknown parameters. In Sect.3, we describe the chemical evolution model that we use to deduce from the cosmic SFR the expected evolution of the abundances of various chemical elements in star-forming structures. We show that the three scenarios considered in the paper for the cosmic SFR are compatible with a large set of observations, hence validating the present model. In § 4.2, we show how the model can be extended to heavy elements produced by the r-process. In Sect. 4, we present the predicted cosmic evolution of Eu, assuming either the CCSN or the NSM as the main astrophysical site of the r-process. We make a detailed comparison with observations at low metallicities which correspond to the early evolution in the Universe and appear to be the most discriminative between both sites. In the NSM case, this allows us in addition to constrain the properties of the binary system, in particular coalescence timescale. The resulting lower and upper limits on the merger rate are used in Sect.5 to make predictions for the expected event rate in the horizon of advanced Virgo/LIGO, as well as for the kilonova rate in future surveys. Finally, we draw our conclusions in Sect. 6.

2 PREDICTING THE NSM RATE

2.1 The cosmic star formation rate (SFR)

The cosmic SFR is a key ingredient to model the rate of stellar explosive events, such as CCSN and NSM. The redshift evolution of the SFR density is now rather well constrained by many observations. Recent data from the Hubble Ultra Deep Field have significantly extended the range of redshift for its determination, from redshift $z = 4$ up to 10 (Bouwens et al. 2007; Bouwens et al 2008, 2011, 2014; Oesch et al. 2012, 2013, 2014). Even more recent observations of high z galaxies and GRBs tend to favor a large amount of still unseen SFR at $z > 9$ (Kistler et al. 2013; Wang 2013). This last study suggests that SFR density may only decline out at $z = 11$ and that GRBs may be useful in exploring the unseen faint dwarf galaxies at high redshift. Behroozi et al. (2013) re-analyzed the average star formation histories from $z = 0$ to 8 and obtained consistent results with observed galaxy stellar mass functions, specific star formation rates and SFR. Moreover, high-redshift galaxy evo-

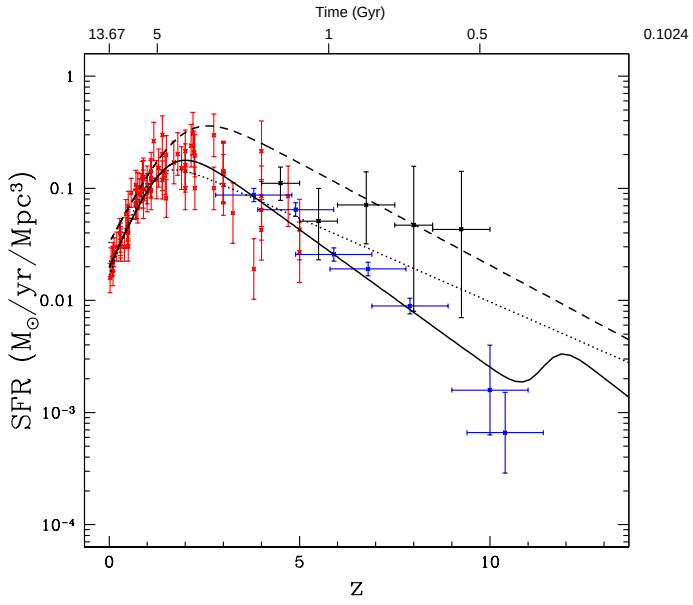


Figure 1. Cosmic SFR as a function of redshift. Three SFR modes considered in the paper, SFR1 (solid line), SFR2 (dotted line) and SFR3 (dashed line). Observations are taken from Behroozi et al. (2013) (red points), Bouwens et al (2014); Oesch et al. (2014) (and references therein) (blue points) and Kistler et al. (2013) (black points).

lution has also been predicted by Behroozi & Silk (2015) who, including recent constraints (Behroozi et al. 2013; Oesch et al. 2013; Kistler et al. 2013; Trenti et al. 2013), probed the unobserved $z > 8$ galaxy populations. The resulting observationally constrained SFR is illustrated in Fig. 1 as a function of the redshift. The corresponding evolution of the cosmic SFR density as a function of redshift can be parametrized by the following form proposed by Springel & Hernquist (2003),

$$\psi(z) = \nu \frac{a \exp[b\,(z - z_m)]}{a - b + b \exp[a\,(z - z_m)]}\,, \tag{1}$$

where ν (in $M_\odot$/yr/Mpc^3) and z_m correspond to the astration rate and the redshift at the SFR maximum, respectively, while b and $b - a$ fix the SFR slope at low and high redshifts, respectively.

Due to the fundamental importance of the SFR in predicting the stellar explosive event rates, and more generally the cosmic chemical evolution, we consider in the present paper three SFR modes (see Fig. 1), which coincide at low redshift, where they reproduce the available data, and differ at high redshift, taking into account the current uncertainties:

- SFR1 includes a standard mode of population (Pop) II/I stars formation between 0.1 and 100 $M_\odot$, and additionally a Pop III stellar mode at high redshift between 36 and 100 $M_\odot$. The corresponding parameters for each mode in Eq. (1) are, respectively, $\nu = 0.18$ and 0.0025, $z_m = 2.0$ and 12.0, $a = 2.37$ and 4.0, and $b = 1.80$ and 3.36.
- SFR2 includes a unique mode of star formation between 0.1 $M_\odot$ and 100 $M_\odot$, with the following parameters: $\nu = 0.15$, $z_m = 1.7$, $a = 2.8$, $b = 2.45$;
- SFR3 also includes a unique mode of star formation between 0.1 $M_\odot$ and 100 $M_\odot$, with the following parameters: $\nu = 0.36$, $z_m = 2.6$, $a = 1.92$, $b = 1.5$.

For each mode, the IMF slope is set to the Salpeter value, i.e. $x = 1.35$.

Star formation is assumed to start at the initial time of $t_0 = 100$ Myr corresponding to a redshift of $z = 30$. We adopt the following cosmological parameters, $\Omega_m = 0.27, \Omega_\Lambda = 0.73$ and $H_0 = 71$ km/s/Mpc (h = 0.71) and a primordial power spectrum with a power-law index $n = 1$. The age t of the Universe is then related to the redshift by

$$\frac{\mathrm{d}t}{\mathrm{d}z} = \frac{9.78\,h^{-1}\,\mathrm{Gyr}}{(1+z)\left[\Omega_\Lambda + \Omega_\mathrm{m}(1+z)^3\right]^{0.5}}\,. \tag{2}$$

As seen in Fig. 1, the SFR2 mode is an intermediate case, whereas SFR1 and SFR3 are respectively close to the lower and higher values of the current measurements at high redshift. We checked that each of these three scenarios is compatible with a large set of independent observational constraints discussed in Sect. 3.2, especially the Thomson optical depth to the cosmological microwave background (CMB) and the cosmic evolution of [Fe/H]. This led to the inclusion of the additional Pop III component at high redshift in the SFR1 case, the standard mode alone being too weak in this case to fulfill the reionization constraint (see Sect. 3.2.1).

2.2 The NSM rate

2.2.1 The CCSN rate and the NS birth rate

Once the evolution of cosmic star formation rate is known, the CCSN rate can be directly deduced if the mass-range of the progenitors is known. We use the predictions from Woosley & Weaver (1995) and assume that the remnant of stars with mass $8 < M/M_\odot < 30$ is a NS, and that more massive stars produce a BH. This leads to the following NS birth rate at time t (related to redshift z by Eq. 2):

$$\dot{R}_\mathrm{NS}(t) = \int \mathrm{d}m\,\Phi(m)\Psi(t_*)\,\Xi_\mathrm{NS}\,(m, Z(t_*))\,, \tag{3}$$

where $\Phi(m)$ is the initial mass function (IMF) integrated over the whole stellar mass range, $\Psi(t)$ the SFR, t_* the formation time of the progenitor, such that $t_* + \tau\,(m, Z(t_*)) = t$, $Z(t_*)$ the metallicity at the epoch of formation of the progenitor, $\tau\,(m, Z(t_*))$ the lifetime of a star formed with mass m and metallicity $Z(t_*)$, and $\Xi_\mathrm{NS}\,(m, Z(t_*))$ is 1 if the stellar remnant is a NS, 0 otherwise. The lifetimes of stars come from (Maeder & Meynet 1989) and the stellar metallicity-dependent remnants are taken from (Woosley & Weaver 1995). The BH birth rate is given by a similar equation, using now $\Xi_\mathrm{BH}\,(m, Z(t_*)) = 1$ if the remnant is a BH, 0 otherwise, and the CCSN rate is the sum of these two rates. The corresponding evolution of these three rates deduced on the basis of SFR1 and SFR2 is plotted in Fig. 2. On the observational point of view, the local CCSN rate is well determined, thanks to large surveys dedicated to the search of supernovae (Mattila et al. 2012). As can be seen in Fig. 2, the agreement with the prediction deduced from the cosmic SFR is good.

2.2.2 The NS merger rate

In contrast to the to the CCSN rate, the astrophysical estimate of compact-binary coalescence rates depends on a number of assumptions and unknown model parameters and are still rather uncertain (Abadie et al. 2010). Among the various estimates, the rate predictions for NS-NS binary systems is the most reliable one since they are based on extrapolations from observed binary pulsars in our Galaxy. These estimates lead to

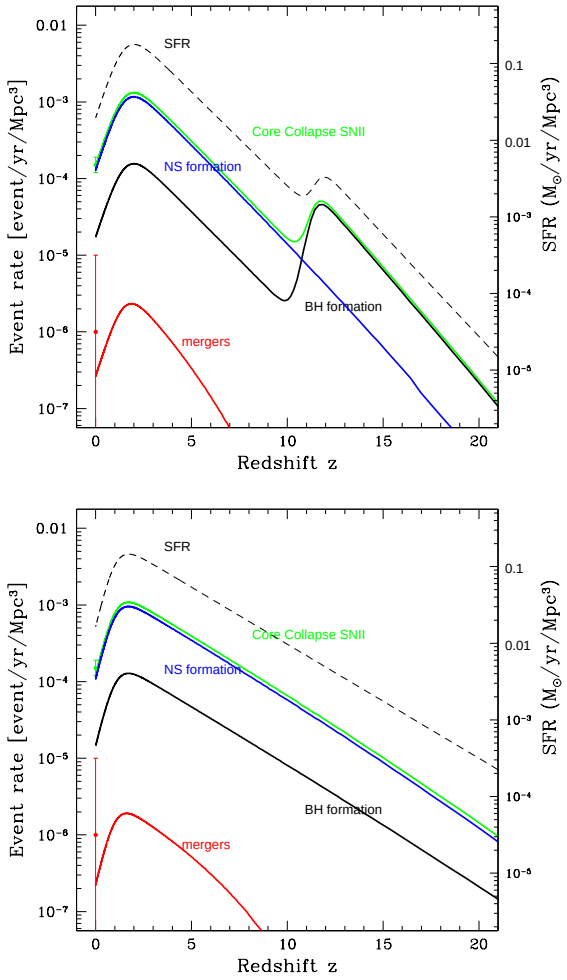


Figure 2. NS and BH birth rates as well as the CCSN and merger rates as a function of the redshift for SFR1 (upper panel) and SFR2 (lower panel). Green and red points represent the local CCSN rate (Mattila et al. 2012) and the total local merger rate (Abadie et al. 2010), respectively. The SFR evolution is also plotted for comparison.

a coalescence rate of about 100 Myr^{-1} per Galaxy, although this rate could plausibly range from 0.1 Myr^{-1} to 1000 Myr^{-1} (Kim et al. 2003; Kalogera et al. 2004; Mennekens & Vanbeveren 2014). Due to the lack of observational data, predictions of the frequency of NS-BH mergers remains even more uncertain and rely exclusively on theoretical studies (Tutukov & Yungelson 1993; Voss & Tauris 2003; O'Shaughnessy et al. 2008; Dominik et al. 2012; Dominik et al. 2013; Mennekens & Vanbeveren 2014; Postnov & Yungelson 2014). These population synthesis models estimate galactic merger rates between 2×10^{-9} and 10^{-5} per year. The range reflects the challenge in comprehensively modelling the formation and evolution of stellar binaries and their remnants. Bauswein et al. (2014) determined an independent upper limit on the merger rate of NS-BH binaries by comparing the predicted r-process nucleosynthesis yields of such systems with the observed galactic amount of r-process material. A strict upper limit of the average NS-BH merger rate of about $6{\times}10^{-5}$ per year was found. Dominik et al. (2013) calculated the cosmological merger rates of NS-NS, NS-BH, BH-BH systems as a function of redshift assuming different SFR histories. While in most cases NS-NS systems dominate the merger rates in the local Universe, BH-BH mergers are found to dominate at high redshift.

In the present study, the merger rate is determined assuming that the formation rate of NS-NS/BH binary systems is a fraction α of the NS birth rate $\dot{R}_{\rm NS}$ and that these binary systems merge after a delay $\Delta t_{\rm NSM}$, the value of which is discussed below. This leads to the following merger rate at time t:

$$\dot{R}_{\rm NSM}(t) = \alpha \dot{R}_{\rm NS}\,(t - \Delta t_{\rm NSM})\ . \qquad (4)$$

In our model, both α and $\Delta t_{\rm NSM}$ and taken as free parameters. The predicted evolution of the merger rate is plotted in Fig. 2 for SFR1 and SFR2, assuming $\alpha = 0.002$ and $\Delta t_{\rm NSM} = 0.2$ Gyr. The independent estimate of the local rate taken from the compilation by Abadie et al. (2010) is indicated for comparison.

2.2.3 *The coalescence timescale*

The coalescence timescale $\Delta t_{\rm NSM}$ is defined as the delay between the formation of the binary system of two NS or a NS and a BH (note that it does not include the lifetime of the two star progenitors of the compact objects). It is a key ingredient as it leads to a different cosmic evolution of NSM compared to CCSN, for which there is no additional delay after the formation of a NS/BH.

The angular momentum loss due to the emission of gravitational waves governs the coalescence timescale. Its value strongly depends on the properties of the binary system, and in particular on the initial separation a (or orbital period T) since $\Delta t_{\rm NSM} \propto a^4$ (resp. $\Delta t_{\rm NSM} \propto T^{8/3}$) (Peters & Mathews 1963, see also Kalogera et al. 2001; Hughes 2009). This dependence leads to an expected broad range of values for $\Delta t_{\rm NSM}$, with however large uncertainties related to the distribution of possible initial orbital parameters in NS/NS and NS/BH binaries (see Hughes 2009, for a recent review). For a binary system of two 1.4 $M_\odot$ NS, the coalescence timescale is $\Delta t_{\rm NSM} = 64$ Myr for $a = 10^{-2}$ AU (resp. $T = 5.2$ h). Only seven NS/NS binary systems are known with measured masses (Lorimer 2005, 2008). The current orbital parameters and the measured masses allow us to estimate the remaining time before the merger. As at least one of the two NS is observed as a pulsar, the measurement of the pulsar period and its time derivative can provide an estimate of the current age of the binary system. The sum of these two timescales gives an estimate of $\Delta t_{\rm NSM}$. Using the values listed in Lorimer (2008), coalescence timescales between 100 and 400 Myr are found in four cases, and values larger than 1 Gyr in the three other cases. The double pulsar PSR J037-3039 corresponds to the lowest value, $\Delta t_{\rm NSM} \simeq 180$ Myr. The famous binary pulsar PSR B1913+16, which has been studied in details for years as a test of general relativity (Hulse & Taylor 1975; Weiberg, Nice and Taylor 2010) is characterised by a coalescence timescale $\Delta t_{\rm NSM} \simeq 420$ Myr.

The distribution of the coalescence timescale can be estimated using a population synthesis code for binary systems, which can be calibrated with observed systems. The result is plotted for two different metallicities in Fig. 3. It has been obtained using the `StarTrack` code described in Belczynski et al. (2002, 2008a), where standard stellar evolution models are implemented with the most updated physics regarding the relevant processes for the evolution of binary systems. Fig. 3 has been produced using the results of a recently updated version of the code (Mink & Belczynski in preparation), including new prescriptions for stellar wind

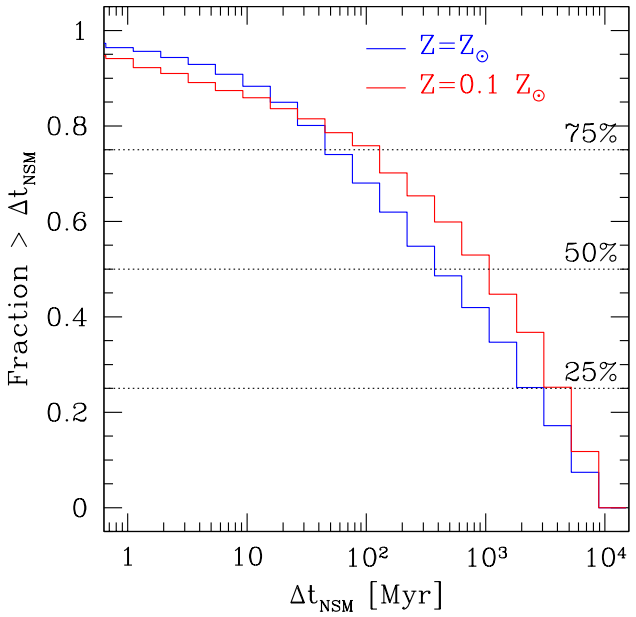


Figure 3. Distribution of the coalescence timescale $\Delta t_{\rm NSM}$ for NS/NS binary systems. The coalescence timescale $\Delta t_{\rm NSM}$ is defined as the delay between the formation of the two NS and the final merger. The plot shows the fraction of mergers with a coalescence timescale above a given value in Myr, for two different metallicities. This distribution has been obtained from an updated version of the population synthesis model described in Belczynski et al. (2002). It covers a broad range of values with a distribution falling approximately like $p(\Delta t_{\rm NSM}) \propto \Delta t_{\rm NSM}^{-1}$.

mass loss rates (Vink etal. 2011; Vink & Grafener 2012), for supernova models (Fryer et al. 2012), for the common envelop phase (Dominik et al. 2012), adding electron capture supernovae for NS formation (Belczynski et al. 2008a), and taking into account recent observational constraints on massive stars in binary systems (Sana etal. 2012). Additionally, the evolutionary model included in the code does not allow for the progenitors to undergo a common-envelope phase while one of the massive binary stars is evolving through the Hertzsprung gap (see Belczynski et al. 2007, for more details). This corresponds to a conservative assumption and additional NS-NS mergers may form if this assumption is relaxed. Compared to the results of Belczynski et al. (2002), this updated calculation predicts a fraction of undetected galactic merging NS-NS systems significantly smaller, now at the level of $\sim$ 10 %. As illustrated in Fig. 3,

the distribution of coalescence timescales predicted by such a detailed calculation shows a broad range of values: at solar metallicity $Z = Z_\odot$ (resp. at metallicity $Z = 0.1Z_\odot$), it is found that 29% (resp. 28%) of systems have $\Delta t_{\rm NSM} \leqslant 100$ Myr, 13% (resp. 16%) have $100 < \Delta t_{\rm NSM} \leqslant 300$ Myr, 15% (resp. 14%) have $0.3 < \Delta t_{\rm NSM} \leqslant 1$ Gyr, 17% (resp. 16%) have $1 < \Delta t_{\rm NSM} \leqslant 3$ Gyr, and 26% (resp. 26%) have $\Delta t_{\rm NSM} > 3$ Gyr. The impact of the metallicity is small. It appears clearly that a significant fraction of systems has a coalescence timescale of a few 100 Myr or less. These systems may dominate the early evolution of the NS merger, and therefore the evolution of Eu at redshift discussed in Sect. 4.

3 COSMIC CHEMICAL EVOLUTION

3.1 Model description

In addition of the rates of explosive events (CCSN, NSM) discussed in the previous sections, the predicted chemical evolution can also be deduced from the cosmic evolution of the SFR. We use the model developed by Daigne et al. (2006); Rollinde et al. (2009); Vangioni et al. (2014), which is based on a hierarchical model for structure formation (Press & Schechter 1974; Sheth & Tormen 1999; Jenkins et al. 2001; Wyithe & Loeb 2003). We assume that the minimum mass of dark matter haloes for star-forming structures is $10^7\ M_\odot$.

Finally, for a given evolution of the cosmic SFR density, as discussed in § 2.1, the model follows the evolution of baryons in the Universe in terms of two main reservoirs. The first is associated with collapsed structures and is divided in two sub-reservoirs: the ISM gas (mass $M_{\rm ISM}(t)$) and the stars and their remnants (mass $M_*(t)$). The second reservoir, the intergalactic medium (IGM, mass $M_{\rm IGM}(t)$), corresponds to the medium in between the collapsed structures. The evolution of the baryonic mass of these reservoirs is governed by a set of differential equations:

$$\frac{dM_{\rm IGM}}{dt} = -\frac{dM_{\rm struct}}{dt} = -a_{\rm b}(t) + o(t), \tag{5}$$

$$\frac{dM_*}{dt} = \Psi(t) - e(t) \text{ and } \frac{dM_{\rm ISM}}{dt} = \frac{dM_{\rm struct}}{dt} - \frac{dM_*}{dt}\ . \tag{6}$$

In addition, we have $M_{\rm ISM}(t) + M_*(t) = M_{\rm struct}(t)$, corresponding to the total baryonic mass of the structures, and $M_{\rm IGM}(t) + M_{\rm struct}(t) =$ constant (total baryonic mass of the Universe).

As can be seen, these equations are controlled by four rates which represent four fundamental processes: the formation of stars through the transfer of baryons from the ISM, $\Psi(t)$, which is directly fixed by the assumption SFR1, 2 or 3 discussed in § 2.1; the formation of structures through the accretion of baryons from the IGM, $a_{\rm b}(t)$; the ejection of enriched gas by stars, $e(t)$ and the outflow of baryons from the structures into the IGM, $o(t)$.

In the model, we track the chemical composition of the ISM and the IGM as a function of time or redshift. The differential equations governing the evolution of the mass fraction $X_i^{\rm ISM}$ ($X_i^{\rm IGM}$) of element i in the ISM (IGM) are given by equations (6) and (7) in section 2 in Daigne et al. (2004).

The baryon accretion rate, $a_{\rm b}(t)$ is computed in the framework of the hierarchical scenario of structure formation and the baryon outflow rate, $o(t)$, from the structures includes a redshift-dependent efficiency, which accounts for the increasing escape velocity of the structures as the galaxy assembly is in progress.

We use the framework of the hierarchical scenario where small structures are formed first. At redshift z, the comoving density of dark matter halos in the mass range $[M, M + dM]$ is $f_{\rm PS}(M, z)dM$, with

$$\int_0^\infty dM\ M f_{\rm PS}(M, z) = \rho_{\rm DM}\ , \tag{7}$$

where $\rho_{\rm DM}$ is the comoving dark matter density. The distribution function of halos $f_{\rm PS}(M, z)$ is computed using the method described in Jenkins et al. (2001). We adopt a rms amplitude $\sigma_8 = 0.9$ for mass density fluctuations in a sphere of radius 8 h^{-1} Mpc. We assume that the baryon distribution traces the dark matter distribution without any bias so that the density of baryons is just proportional to the density of dark matter by a factor $\Omega_b/(\Omega_m - \Omega_b)$.

The fraction of baryons at redshift z which are in such structures is given by

$$f_{\rm b,struct}(z) = \frac{\int_{M_{\rm min}}^{\infty} dM\, M f_{\rm PS}(M,z)}{\int_{0}^{\infty} dM\, M f_{\rm PS}(M,z)} \,. \quad (8)$$

Therefore, the mass flux $a_{\rm b}$ can be estimated by

$$a_{\rm b}(t) \;=\; \Omega_{\rm b}\left(\frac{3H_0^2}{8\pi G}\right)\left(\frac{dt}{dz}\right)^{-1}\left|\frac{d f_{\rm b,struct}}{dz}\right| . \quad (9)$$

In addition to the NS and BH birth rates, the CCSN rate, and the NS-NS and NS-BH merger rates discussed in § 2.2 (and of special interest in the present study), several other quantities are followed as a function of the redshift z, namely the WD birth rate, the type Ia supernova rate, the abundances of various chemical elements, including Fe and Eu, in the ISM and the IGM, the ionizing flux from stars, the ionization state of the IGM and the Thomson optical depth of the CMB. A detailed description of this cosmic evolution model can be found in Daigne et al. (2006); Rollinde et al. (2009); Vangioni et al. (2014).

3.2 Observational constraints on the chemical evolution model

We tested that each cosmic evolution scenario discussed in this paper fulfills two important observational constraints, namely the observed cosmic evolution of [Fe/H] (corresponds to the logarithm of the abundance of iron normalized to the solar one) and the measured Thomson optical depth of the CMB. Following the detailed analysis presented in Vangioni et al. (2014) for different possible SFR using the same cosmic evolution model, this leads to the choice of the three SFRs presented in § 2.1. The SFR1 and SFR2 cases are directly taken from their study.

SFR1 corresponds to a standard SFR with an additional Pop III star component at high redshift, mainly motivated by the fact that the ionizing flux at high redshift produced by the standard mode only is not large enough to reproduce the Thomson optical depth of the CMB (see § 3.2.1).

SFR2 is a SFR enhanced at high z. The third mode considered here, SFR3, is chosen as the upper limit of the SFR at high redshift obtained from the constraint of the Thomson optical depth of the CMB (see Fig. 4). As shown in Fig. 1, SFR1 fits the observational constraints from Behroozi et al. (2013); Bouwens et al (2014) and Oesch et al. (2014), whereas SFR2 and SFR3 take into account the studies of (Trenti et al. 2013) and Kistler et al. (2013), respectively.

3.2.1 Reionization

Concerning the ionization history, the evolution of the volume filling fraction $Q_{\rm ion}(z)$ of ionized regions at redshift z is given by

$$\frac{{\rm d}Q_{\rm ion}(z)}{{\rm d}z} = \frac{1}{n_{\rm b}}\frac{{\rm d}n_{\rm ion}(z)}{{\rm d}z} - \alpha_{\rm B} n_{\rm b} C(z) Q_{\rm ion}^2(z)\,(1+z)^3\left|\frac{{\rm d}t}{{\rm d}z}\right| , \quad (10)$$

where $n_{\rm b}$ is the comoving density in baryons, $n_{\rm ion}(z)$ the comoving density of ionizing photons, $\alpha_{\rm B}$ the recombination coefficient, and $C(z)$ the clumping factor. This last factor is taken from Greif & Bromm (2006) and varies from a value of 2 at $z \leqslant 20$ to a constant value of 10 for $z < 6$. The escape fraction, $f_{\rm esc}$, is set to 0.2 for each of our SFR modes. The number of ionizing photons emitted by massive stars is calculated using the tables given in (Schaerer 2002). Finally, the Thomson optical depth between redshifts $z' = 0$ and z is computed following (Greif & Bromm 2006), i.e.

$$\tau = c\,\sigma_{\rm T}\,n_{\rm b}\int_0^z {\rm d}z'\; Q_{\rm ion}(z')\,(1+z')^3\left|\frac{{\rm d}t}{{\rm d}z}(z')\right| , \quad (11)$$

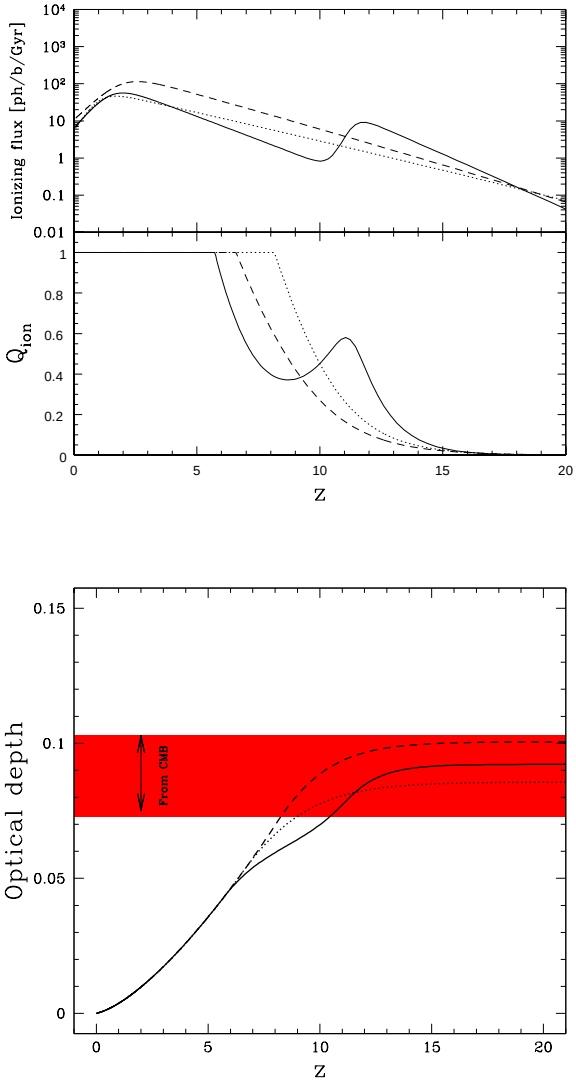


Figure 4. Reionisation. Evolution as a function of redshift of the ionizing flux (top panel), volume filling fraction $Q_{\rm ion}$ (middle panel) and Thomson optical depth (lower panel) for the three SFR modes (conventions are the same as in Fig. 1). WMAP9 results for the optical depth at high redshift (Hinshaw et al. 2013) are indicated by a red strip in the lower panel.

where $\sigma_{\rm T}$ is the Thomson scattering cross section. Fig. 4 shows the evolution of the volume filling fraction $Q_{\rm ion}$ and the ionizing flux for the three SFR histories, and the resulting Thomson optical depth, the value of which is found to agree well with the measurement from CMB observations by WMAP9 (Hinshaw et al. 2013) at high redshift. As mentioned above, the SFR1 scenario without the Pop III mode at high redshift would not fulfill this constraint (Vangioni et al. 2014) and SFR3 is adjusted to reproduce the upper limit on the optical depth. Note that the last results from the Planck Collaboration (2014, 2015) give a revised Thomson optical depth $\tau = 0.079 \pm 0.017$. This value is lower than the WMAP9 one ($\tau = 0.089 \pm 0.014$). Consequently, in this context, the contribution of Pop III stars in the SFR1 model should be lowered.

3.2.2 Cosmic chemical evolution: iron

Our model includes the stellar lifetimes estimated by Maeder & Meynet (1989) for intermediate mass stars with $0.9 < M/M_\odot < 8$ and by Schaerer (2002) for more massive stars. Lifetimes of low mass stars ($M/M_\odot < 0.9$), such as the old halo stars where abundances of Eu are measured at low metallicity, are long enough for the star to be still observed today, whatever the redshift of formation. Stars formed at redshift z inherit their initial chemical composition from the abundances in the ISM at the same redshift. Thus, the observed abundances in stars reflect, in a somewhat complex way, the yields of all massive stars that have exploded earlier. The stellar yields adopted in our model depend on the stellar mass and metallicity. By default, we use the tables of yields from (Woosley & Weaver 1995) for massive stars ($8 < M/M_\odot < 40$). An interpolation is made between the different metallicities ($Z = 0$, $0.0001Z_\odot$, $0.001Z_\odot$, $0.1Z_\odot$ and $Z_\odot$) and masses, and tabulated values are extrapolated for stars beyond $40\,M_\odot$, which correspond to a small fraction of the population of massive stars (i.e. $(40^{-x} - 100^{-x}) / (8^{-x} - 100^{-x}) \simeq 8\%$ for the Salpeter IMF of index $x = 1.35$).

Fig. 5 shows the [Fe/H] evolution as a function of time and redshift for the three SFR modes. Data correspond to chemical abundance determinations in about 250 damped Lyα (DLA) systems (Rafelski et al. 2012, and references therein) as a function of the redshift. In their paper, they present 47 DLA systems at $z > 4$ observed with the Echellette Spectrograph and Imager and the High Resolution Echelle Spectrometer on the Keck telescopes (for more details see Vangioni et al. 2014). We use Eq. (2) to associate a time with the observed redshift for each observed DLA system. As illustrated in Fig. 5, the cosmic evolution of the iron abundance is reproduced by each of the three scenarios, passing through the upper limit of the points. However, note that these iron abundances are measured in the gas phase which should be considered as lower limits due to depletion into grains in the ISM. As seen in Fig. 5 (middle panel), the early iron evolution depends strongly on the shape of the SFR at high z. In particular, it can be seen that a cosmic [Fe/H] $= -4$ enrichment is achieved at the very beginning, $\Delta t = t - t_0 \simeq 0.015$ Gyr for SFR2, 0.05 Gyr for SFR3, and 0.4 Gyr for SFR1. This time delay in the early Fe enrichment can have a drastic impact on the interpretation of the early cosmic chemical evolution with respect to observations, as discussed in Sect. 4.

3.2.3 Cosmic chemical evolution: other elements

As detailed in Vangioni et al. (2014), the present cosmic evolutionary model has been used to predict the "standard" chemical evolution of light elements, such as C, N, O or Mg and to test its predictive power with respect to available observations (Suda et al. 2008, 2011). The sensitivity to different SFR has also been explored.

- *Carbon, oxygen.* It was found that the [C/H] evolution as a function of the iron abundance is essentially independent of the adopted SFR model for [Fe/H] > -2 or $z < 4$. At higher z (lower metallicity), the SFR including a Pop III mode (like SFR1) was shown to be in better agreement with the observation of ultra-metal-poor carbon-enhanced stars, which presents a significant dispersion. Similar conclusions were drawn for the oxygen evolution, where the Pop III contribution to the SFR1 model allows for a high production of O at low metallicities with a local peak in [O/H] at [Fe/H] ≈ -4.8. Interestingly, this model can also explain the oxygen abundances in ultra-low-metallicity stars (see in particular Fig. 9 in Vangioni et al. 2014).

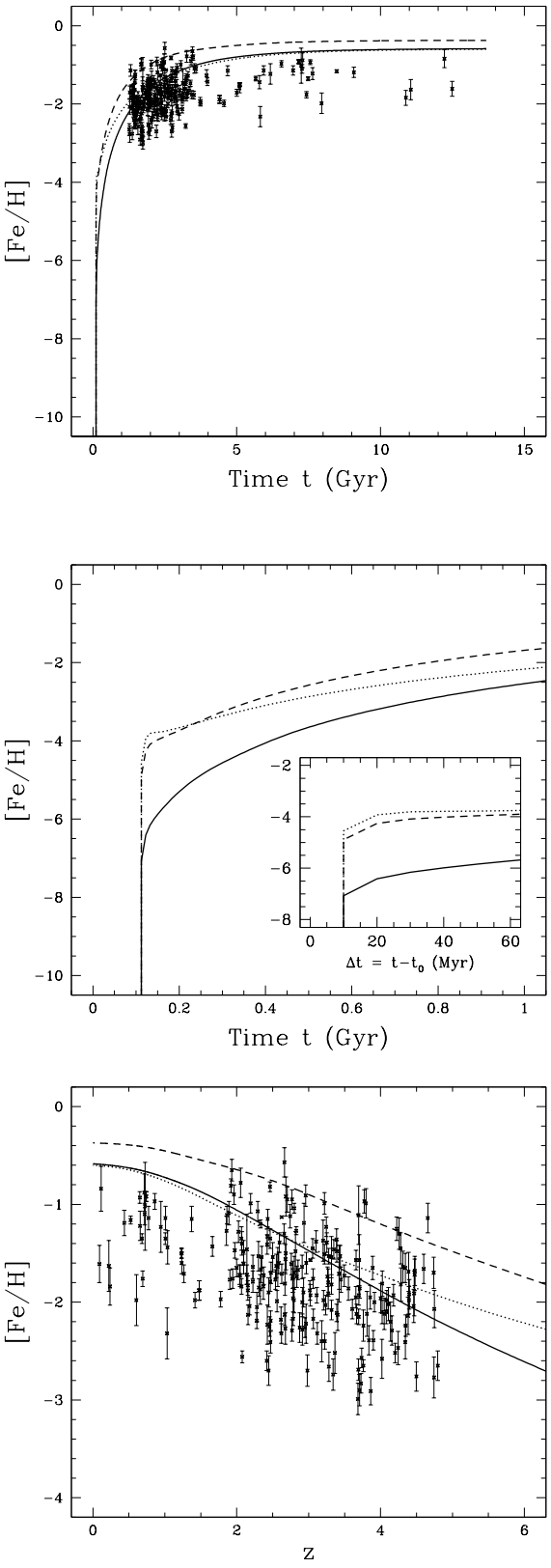


Figure 5. Iron evolution. [Fe/H] evolution as a function of time t (upper panels) or redshift z (lower panel) for the three SFR modes (lines are the same as defined in Fig. 1). The middle panel focusses on the early time evolution, with the insert emphasizing the three different time delays around the [Fe/H]=-4 iron enrichment . Data correspond to DLAs observations as a function of redshift (Rafelski et al. 2012). Eq. (2) is used to convert z into

• *Magnesium.* As in the oxygen case, the inclusion of a high-mass model in SFR1 at large redshift directly impacts the evolution of Mg in star forming structures. The predicted Mg pattern in the SFR1 case is, however, not observed at low metallicity (see Fig. 10 in Vangioni et al. 2014). However, new studies in high mass stars show that Mg evolution at low metallicity remains sensitive to the predicted nucleosynthesis in massive zero-metallicity stars. Such calculations have been recently revisited by Heger & Woosley (2010) who showed that in their models no Mg is produced in zero-metallicity stars more massive than 30 $M_{\odot}$. In this case, the early production of Mg in the three SFR cases discussed here is found to reproduce well the bulk of data, as shown in Figure 10b of Vangioni et al. (2014).

• *Local stellar metallicity distribution function (MDF).*

We show in Fig. 6 the MDF derived by An et al. (2013) using the SDSS photometric Catalogue together with our computed MDF based on the SFR1 mode (the other modes giving very similar results). As found by An et al. (2013), the in-situ photometric metallicity distribution has a shape that matches that of the kinematically-selected local halo stars from Norris and Ryan (1991). For this reason, we adopt their SDSS calibration catalog MDF as a reference since it presents the advantage of expressing the MDF directly as a function of [Fe/H]. The global shape of our computed MDF is shown in Fig. 6 to be in good agreement with the observation. We point out here the impact of the choice of the iron yields and the related uncertainties. We present four curves reflecting uncertainties mainly related to the CCSN mass cut. The blue curve corresponds to the standard yields from Woosley & Weaver (1995) adopted in the rest of the paper, which are varying with metallicity, the green curve to the same yields divided by a factor 2, the dot-dash black curve to yields calculated from solar metallicity stars only, and the red curve to Fe yields determined by Kobayashi et al. (2006).

• *Stellar mass.* As shown by Vangioni et al. (2014), the cosmic evolution of the stellar mass as a function of the redshift is also found to be in good agreement with cosmological observational photometric data (see their Fig. 12b), in particular for the SFR1 mode.

In conclusion, based on the previous study of Vangioni et al. (2014) within the same cosmological context and on the basis of the same SFR cases, it can be concluded that the standard chemical evolution is rather well reproduced by the cosmic evolution of the star formation considered in the present study, and consequently that the present model is well suited to describe the averaged chemical history. The evolution of Milky Way-like galaxies appears to be not far from the averaged history. As discussed recently in Frebel and Norris (2015), this opens the possibility of "near-field cosmology" based on stellar archeology, especially using the population of the oldest stars in the halo of our Galaxy and in dwarf galaxies. We will use this approach in the next Section to study the cosmic evolution of r-process elements.

4 COSMIC EVOLUTION OF R-PROCESS ELEMENTS

As far as the galactic chemical evolution is concerned, CCSN remain promising sites, especially in view of their potential to significantly contribute to the galactic enrichment (Argast et al. 2004). However, they remain handicapped by large uncertainties associated mainly with the still incompletely understood mechanism that is responsible for the supernova explosion and the persistent difficulties to obtain suitable r-process conditions in self-consistent

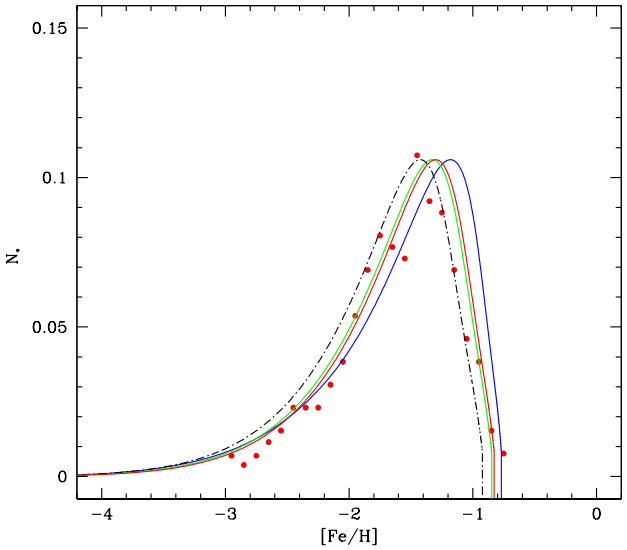


Figure 6. Local metallicity distribution function, i.e. normalized number of stars as a function of the iron abundance [Fe/H]. The MDF is calculated with SFR1 mode and the red circles to the observed MDF deduced by (An et al. 2013) using SDSS photometry. We present four curves obtained with different Fe yields reflecting uncertainties mainly related to the CCSN mass cut. Blue curve : standard yields from (Woosley & Weaver 1995) with yields varying with metallicity, green curve : same after dividing these yields by a factor 2, dot-dash black curve : same using only yields calculated from solar metallicity stars only, red curve : same when using the iron yields determined by (Kobayashi et al. 2006).

dynamical explosion and neutron-star cooling models (Janka 2012; Hüdepohl et al. 2010; Fischer et al. 2010). In addition, nucleosynthesis predictions of the detailed composition of the ejected matter remain difficult due to the remarkable sensitivity of r-process calculation to the still unknown initial properties of the ejecta.

In contrast, NS-NS or NS-BH mergers, which today are clearly favored from a nucleosynthesis point of view, have been claimed to be ruled out as the dominant r-process source by early studies on the basis of inhomogeneous chemical evolution models (Argast et al. 2004), due to their low rates of occurrence which seem to be inconsistent with observations of low-metallicity r-process-rich stars. In addition, the significant amount of r-process material ejected by a single NSM leads to a large scatter in r-process enrichment at later times that does not seem to be confirmed by observations.

Recent studies (Matteucci et al. 2014; Komiya et al. 2014; Cescutti & Chiappini 2014; Mennekens & Vanbeveren 2014; Tsujimoto & Shigeyama 2014a,b; Shen et al. 2014; van de Voort et al. 2015; Ramirez-Ruiz et al. 2015) have reconsidered the chemical evolution of r-process elements in different evolutionary contexts, and reached rather different conclusions. More specifically, Matteucci et al. (2014) explored the Eu production in the Milky Way using a local chemical evolution model. Their observational constraints at low metallicity come essentially from the observations of Eu in metal-poor stars by François et al. (2007), without including the related error bars and upper limits. The relevance of the NSM scenario on the production of Eu has been studied by testing the effect of *(i)* the coalescence timescale

of the binary system *(ii)* the Eu yield expected to be ejected from NSM and *(iii)* the range of the initial mass of the NS progenitors. Similarly, the CCSN scenario has been explored by considering different possible Eu yields assuming a strong r-process taking place in CCSN. In this framework, NSM is found to be potentially a major r-process source if the coalescence timescale is of the order of 1 Myr and the ejected Eu yield of the order of 3×10^{-7} $M_\odot$ for a mass range of progenitors of NS ranging between 9 and 50 $M_\odot$. The scenario where both CCSN and NSM contribute to the Eu synthesis is also compatible with observations provided NSM produce 2×10^{-7} $M_\odot$ of Eu per system and each CCSN with progenitors in the range of 20–50 $M_\odot$ produce around $10^{-8} - 10^{-9}$ $M_\odot$ of Eu.

In parallel, Komiya et al. (2014) investigated the chemical enrichment of r-process elements using a hierarchical galaxy formation model. The CCSN scenario is found to reproduce the scatter of observed r abundances in low metallicity stars if about 10% of CCSN in the low-mass end (i.e. for progenitor mass of the order of 10 $M_\odot$) is the dominant r-process source and the star formation efficiency amounts to about 0.1 per Gyr. For NSM to be the main r-process site, a coalescence timescale of about 10 Myr with an event rate about 100 times larger than currently observed in the Galaxy need to be considered.

We note that the coalescence timescale in the studies by Matteucci et al. (2014) and Komiya et al. (2014) is constrained to be surprisingly short compared to known systems in our Galaxy and theoretical predictions by stellar population models (see Sect. 2.2.3).

Cescutti & Chiappini (2014) computed inhomogeneous chemical evolution models for the galactic halo, taking into account the contribution of electron-capture and magnetorotationally driven supernovae (including fast-rotating progenitors), but not NSM, to explain the Eu scatter in metal-poor stars.

Mennekens & Vanbeveren (2014) also studied the temporal evolution of the galactic population of double NS binaries, mixed systems with a NS and BH component, and double BH binaries. They conclude that, except for the first 100 Myr of the evolutionary phase of the Galaxy, double compact star mergers may be the major production sites of r-process elements, and it is probable that the mixed NS-BH systems dominate over double NS binary mergers.

Finally, Shen et al. (2014) and van de Voort et al. (2015) estimated the enrichment history of r-process elements in the Galaxy, as traced by the [Eu/Fe] ratio, using a high resolution cosmological zoom-in simulation. Unlike previous studies, it was found that the nucleosynthetic products from compact binary mergers can be incorporated into stars of very low metallicity and at early times, even with a minimum time delay of 100 Myr and that compact binary mergers could be the dominant source of r-process nucleosynthesis.

In the present Section, we bring our own contribution to this difficult debate. We first summarize the available Eu observations and then propose a detailed comparison with our predictions of the Eu evolution along the cosmic history, using the three possible cosmic SFR density discussed in § 2.1.

4.1 Eu: observations

We have gathered most of the recent observations on Eu abundance (Eu/H and [Eu/Fe] as a function of [Fe/H]) in metal poor stars (François et al. 2007; Honda et al. 2004; Barklem et al. 2005; Simmerer et al. 2004; Roederer 2011; Roederer et al. 2010, 2012, 2014a,b,c; Ren et al. 2012; Worley et al. 2013) together with the abundances found in dwarf spheroidal systems (Shertone, Côté & Stetson 2001; Shertone, et al. 2003; Geilser et al. 2005; Cohen and Huang 2009; Letarte et al. 2010; Starkenburg et al. 2013; McWilliam et al. 2013). It is interesting to note that the bulk of data coming from external dwarf galaxies is embedded in galactic ones. The solar abundances are taken from Lodders (2003).

The determination of Eu abundance suffers from the fact that only few transitions are visible in the spectrum of metal poor stars. The strongest transitions are rather weak and it becomes particularly difficult to detect and estimate the abundance of this element at low metallicities. Typically, the strongest Eu line becomes almost undetectable below [Fe/H] $\simeq -3.5$. The detection or the non-detection depends on the S/N ratio of the spectrum, on the presence or not of an overabundance of Eu in a given star and finally on the temperature and gravity of the star. This situation clearly shows up in the diagrams where the number of true detection of Eu at very low metallicity are only a handful. Moreover, due to the scarcity of very metal poor stars in the halo, the new very metal poor candidates are faint and require a significant fraction of observing time on 10 m class telescopes. Consequently, the number of stars with [Fe/H] $\simeq -3.5$ for which the Eu abundance has been measured is small. The sample used in the present paper does not represent an unbiased sample of stars, so the distribution function of [Eu/Fe] vs [Fe/H] has no significance. In several stars, the upper limit of the Eu abundance has been computed. These upper limits are useful as they complement the real measurement and show that, so far, no star below [Fe/H] $\simeq -3.5$ has a very high [Eu/Fe] ratio, i.e. of the order of what is found in stars at [Fe/H] $\simeq -3.5$. Although we cannot fully rule out the existence of such stars with [Eu/Fe] $\geqslant 1.2$ dex, the present sample seems to indicate that the upper envelope of the [Eu/Fe] stops to rise at [Fe/H] $\simeq -3.0$ This hypothesis receives support from the recent study of Hansen et al. (2014) who analyzed 4 stars with [Fe/H] $\leqslant -4.00$ and did not report any measurement of the Eu abundance although the wavelength range of the spectra used in this study covers the Eu transitions wavelength.

The inspection of observed abundances (see Fig. 7) shows the apparent existence of two branches starting below [Fe/H] $\simeq -2.5$, the first one with high values of [Eu/Fe] as high as +2.0, the second one with decreasing values down to [Eu/Fe] $\simeq -1.0$ at [Fe/H] $\simeq -3.2$. As the sample is biased, it is difficult to be fully confident about the reality of this two branches. The plot could also well be interpreted as an increase of the dispersion as the metallicity decreases. Indeed, semi analytic models of merger tree which trace the chemical evolution of matter in different regions of the Universe (from over- to under-dense regions) show clearly a dispersion growing as a function of the redshift (Dvorkin et al. 2015).

The origin of the stars with a high level of r-process elements like Eu is still a matter of debate. A recent analysis by Roederer et al. (2014b,c) has shown and confirmed that this overabundance is also found in main-sequence turn-off stars rejecting the hypothesis that the star would have produced itself such overabundances. They also did not find any compelling evidence to suggest that a noticeable high fraction of highly r-process enriched stars are members of binary systems, assigning the origin of the r-process enhancement to a companion star. They also confirmed that these peculiar stars do not present a different α-element chemical signature from the bulk of the other metal poor stars. Therefore, the site responsible for the production of this r-process enhancement is not expected to produce any chemical anomalies for light elements.

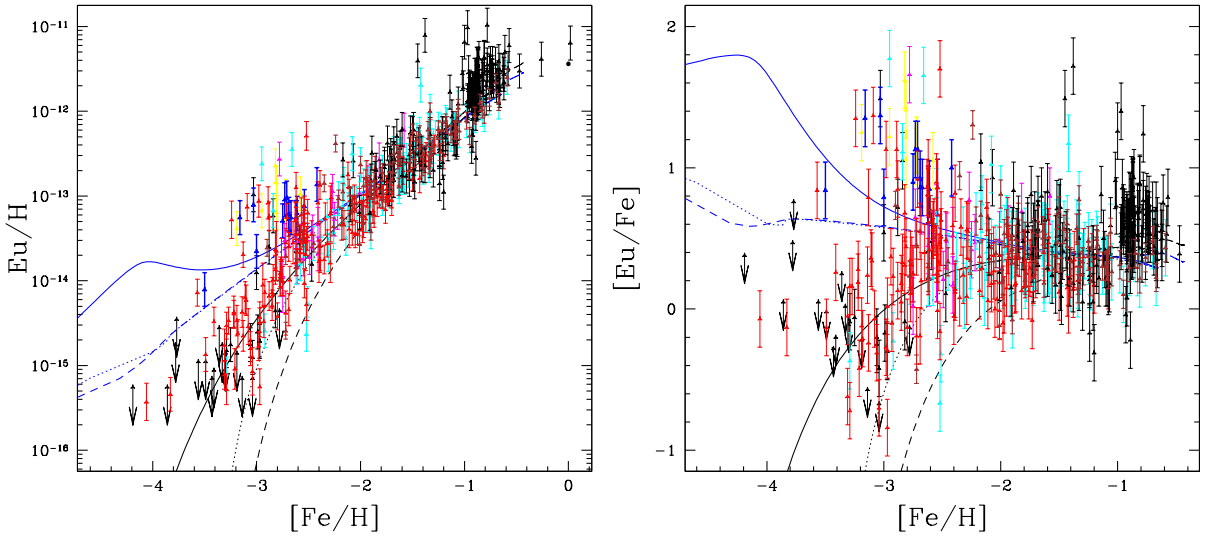


Figure 7. Cosmic evolution of Eu: comparison between the two possible astrophysical sites Eu/H and [Eu/Fe] vs [Fe/H]. Evolution of Eu/H and [Eu/Fe] as a function of [Fe/H] either in the CCSN (blue lines) or in the NSM (black lines) scenario. The evolution is computed for the three SFR modes considered in the present study, SFR1 (solid lines), SFR2 (dotted lines), SFR3 (dashed lines). In the CCSN scenario, the Eu yield is 10^{-7} $M_{\odot}$ per supernova. In the NSM scenario, the Eu yield is 7×10^{-5} $M_{\odot}$ per merger, the fraction of binary compact objects is $\alpha = 0.002$ and the coalescence timescale is $\Delta t_{\rm NSM} = 0.2$ Gyr. Data points come from different references: black points and upper limits at low metallicity from (François et al. 2007), brown points at higher metallicity from (Simmerer et al. 2004), yellow from (Barklem et al. 2005), magenta from (Ren et al. 2012), red from (Roederer et al. 2010, 2014a,b), heavy blue points from (Roederer et al. 2014c). The bulk of black points at high metallicity come from dwarf spheroidal systems (Shertone, Côté & Stetson 2001; Shertone, et al. 2003; Geilser et al. 2005; Cohen and Huang 2009; Letarte et al. 2010; Starkenburg et al. 2013; McWilliam et al. 2013).

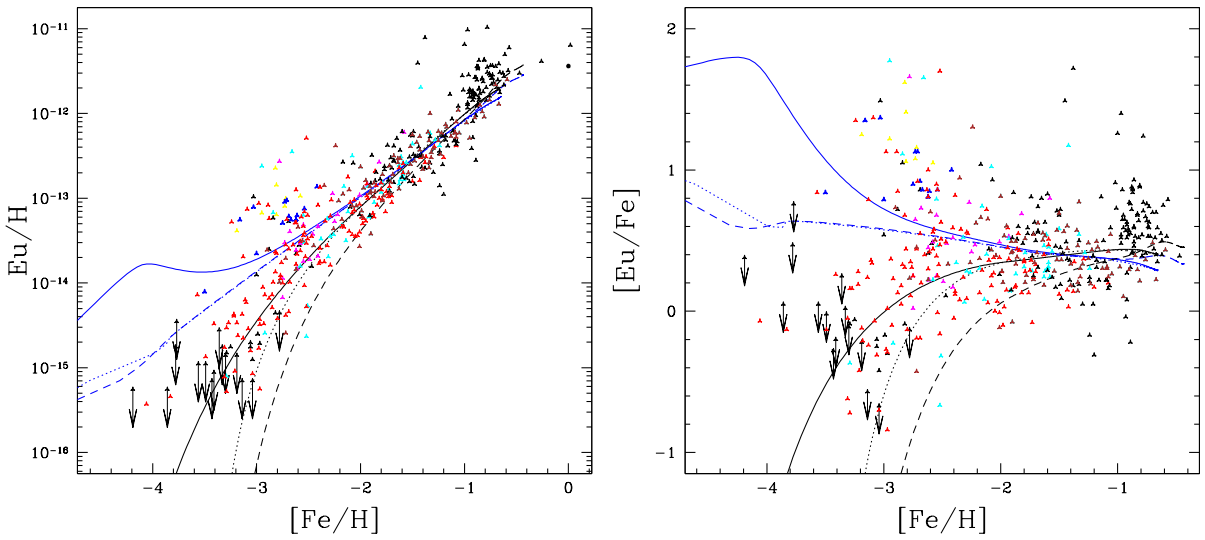


Figure 8. Same as Fig. 7 but without error bars.

4.2 Eu: yields from CCSN and NSM

Each of the two possible r-process sites, CCSN and NSM, may potentially contribute to the galactic r-process enrichment, but we will assume in the present work that they are mutually exclusive, so that the the r-process in the Universe is either originating from CCSN or NSM but not from a mix of both sites. While the cosmic evolution of r-process elements in the CCSN scenario essentially depends on the amount of r-process material ejected by the explosion, in the NSM scenario, it is also function of the binary fraction of compact objects α and the coalescence timescale of the binary system $\Delta t_{\rm NSM}$. We describe here the adopted yields of Eu expected to be ejected from CCSN or NSM.

4.2.1 Eu yields from CCSN

Since there exists so far no consistent r-process calculation in CCSN, the Eu yields from supernovae remain highly uncertain. The CCSN Eu yields are therefore free parameters that can only be adjusted to reproduce some observables, like the [Eu/Fe] trend as a function of the [Fe/H] observed in galactic stars or the total amount of Eu material in the Galaxy. In particular in this latter case, if we assume that the heavy-element composition in the solar system is representative for the whole Galaxy (as suggested by the small scatter of the Eu abundance in the present-day Milky Way), for a Eu mass fraction of 3.7×10^{-10} (Lodders 2003; Asplund et al. 2009) and a total galactic baryonic mass of 6×10^{10} $M_\odot$ (McMillan 2011), this implies a Eu Galactic content of 22 $M_\odot$. Assuming that the CCSN events occur at a constant rate identical to the currently observed one, i.e. about one per century during the approximate age of the Galaxy of 1.3 $\times 10^{10}$ yr, some 1.3 10^8 type-II explosions should be responsible for the 22 $M_\odot$ of Eu, i.e. each CCSN should in this case produce about 1.7×10^{-7} $M_\odot$ of Eu. For this reason, by simplicity, a constant yield of 10^{-7} $M_\odot$ of Eu is adopted here for all CCSN, regardless of the mass of the progenitor.

4.2.2 Eu yields from NSM

While a successful r-process cannot be obtained *ab initio* in CCSN simulations, NSM models consistently predict a significant production and ejection of r-process material. In particular, a mass-weighted combination of the dynamical ejecta from both the binary merger phase and the secular ejecta from the BH-torus evolution has been shown (Just et al. 2015) to reproduce the solar r-abundance pattern, and therefore also the elemental one seen in ultra-metal-poor stars, amazingly well in the whole $90 \lesssim A \leqslant 210$ range. This calculation represents today the most consistent estimate of Eu production by NS-NS and NS-BH mergers taking consistently into account both the prompt ejecta as well as the relic BH-torus outflow contributions. For this reason, the Eu yields obtained in such combined models are considered in the present study. More precisely, the three combined systems (merger model plus remnant model) corresponding to models with torus masses $M_{\rm torus} = 0.03, 0.1$ and 0.3 $M_\odot$ (see Fig. 19 of Just et al. 2015) are found to eject between 7×10^{-5} and 2×10^{-4} $M_\odot$ of Eu. A fiducial Eu yield of 7×10^{-5} $M_\odot$ is adopted here (see the distribution of the ejected mass in NSM mergers in Fig. 6 in Fryer et al. (2015)).

4.3 Eu: cosmic evolution

4.3.1 Evolution of Eu as a function of [Fe/H]

The Eu cosmic evolution is computed for the three SFR modes. Figs. 7 and 8 (with and without error bars) show the predicted evolution of Eu/H and [Eu/Fe] as a function of [Fe/H] for both r-process sites, separately, the CCSN (blue lines) and NSM (black lines), with a comparison to the observations described in Sect. 4.1.

Concerning the CCSN scenario, the Eu yield of 10^{-7} $M_\odot$ is seen to reproduce fairly well the spectroscopic data for [Fe/H] > -2.5. At lower metallicity, Eu is clearly overproduced by CCSN, specifically if we consider Eu data at lowest metallicity, as pointed in Sect. 4.1. In the SFR1 mode, where a Pop III contribution is included, the overproduction is even more significant due to the lack of iron production at very low metallicities in the models of Woosley & Weaver (1995) (Case B), whereas Eu is assumed to be produced in all mass ranges of massive stars.

Regarding the NSM scenario, with the fixed value of 7×10^{-5} $M_\odot$ for the Eu yield (see § 4.2.2), observations at [Fe/H] > -2.5 are seen to be in good agreement with the predicted evolution for a fraction of binary compact objects $\alpha = 0.002$ and a coalescence timescale $\Delta t_{\rm NSM} = 0.2$ Gyr. A larger Eu yield of 2×10^{-4} $M_\odot$ would logically imply a lower value of $\alpha \simeq 0.0007$, both parameters being degenerate in this approach. The agreement with the observations of Eu at low metallicity depends strongly on the coalescence timescale, which can therefore be constrained for each SFR mode, as illustrated in Figs. 9, 10 and 11, where we compare four coalescence time scales $\Delta t_{\rm NSM} = 0$, 0.05, 0.1, 0.2 Gyr for each SFR mode. The best fit is obtained for a typical coalescence timescale of 0.2 Gyr for SFR1 (Fig. 9), 0.1 Gyr for SFR2 (Fig. 10) and 0.05 Gyr for SFR3 (Fig. 11).

The difference stems from the [Fe/H] evolution which differs significantly for the three SFR modes, as already pointed out in § 3.2.2 (see Fig. 5). The more iron produced at early time, the shorter coalescence timescale needed to explain the low-metallicity r-process-rich stars. An important conclusion, illustrated by these results, is that a coalescence timescale larger than typically 0.3 Gyr is excluded by the observations of Eu at low [Fe/H] for all SFR. Note that the production of iron from type Ia supernovae is included in our calculation but their contribution becomes efficient only at the end of the cosmic evolution, i.e. for [Fe/H] $\gtrsim -1$. Indeed, due to the lifetime of the 2 $M_\odot$ stars (2 Gyr) and the potential time delay of explosions, SNIa iron enriches the ISM at $z < 3$. It should also be noted that, contrary to the CCSN case, the Pop III component in the SFR1 mode does not affect the predictions in the NSM scenario due to the time delay of the merging.

4.3.2 Evolution of Eu as a function of redshift

Fig. 12 shows the Eu evolution as a function of redshift for the three SFR modes. To include observational data as a function of z, each [Fe/H] value needs to be associated with a corresponding redshift. In our approach, the iron abundance increases monotonically with time, so that there exists a unique relation between [Fe/H] and z, using equation 1, but this relation is however function of the adopted SFR since the Fe evolution depends on the SFR, as shown in Fig. 5 (lower panel). For this reason, the three modes are shown in different panels. In the NSM scenario, the coalescence timescale adopted for each SFR mode is $\Delta t_{NSM} = 0.2, 0.1, 0.05$ Gyr for SFR1, SFR2, SFR3, respectively, as discussed above.

4.4 Sensitivity analysis

4.4.1 Eu from CCSN and the Pop III star component

As already mentioned, the Eu nucleosynthesis by CCSN remains highly uncertain. In our standard calculations (§ 4.3), it was assumed that each CCSN produces 10^{-7} $M_\odot$ of Eu regardless of the mass and metallicity of its progenitor. If we consider in the SFR1 mode the existence of a Pop III star component, as required to explain the Thomson optical depth of the CMB measured by WMAP9 (see Fig. 4), Fig. 7 clearly shows a large overproduction of Eu at low metallicity. So, would the r-process successfully take place in CCSN, the observation of Eu in ultra-metal-poor star could be a discriminant indicator highlighting the existence or not of Pop III stars. However, if we assume that Pop III stars, or more generally $Z < 10^{-4} Z_\odot$ stars, do not produce r-process elements significantly (less than typically 5 10^{-9} $M_\odot$), the Eu evolution curve in SFR1

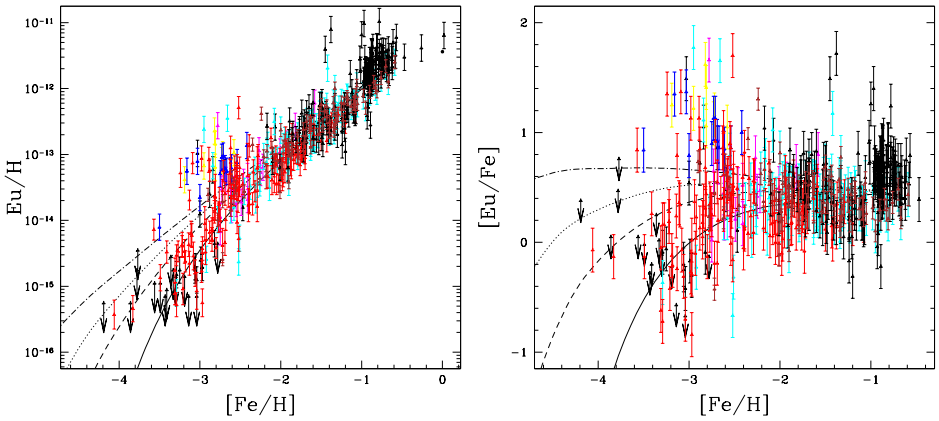


Figure 9. Cosmic evolution of Eu in the NSM scenario: effect of the coalescence timescale (SFR1 case). Same as Fig. 7 in the NSM scenario and SFR1 case. We compare four different coalescence timescales: 0 (dot-dash line), 0.05 (dotted line), 0.1 (dashed line) and 0.2 Gyr (solid line).

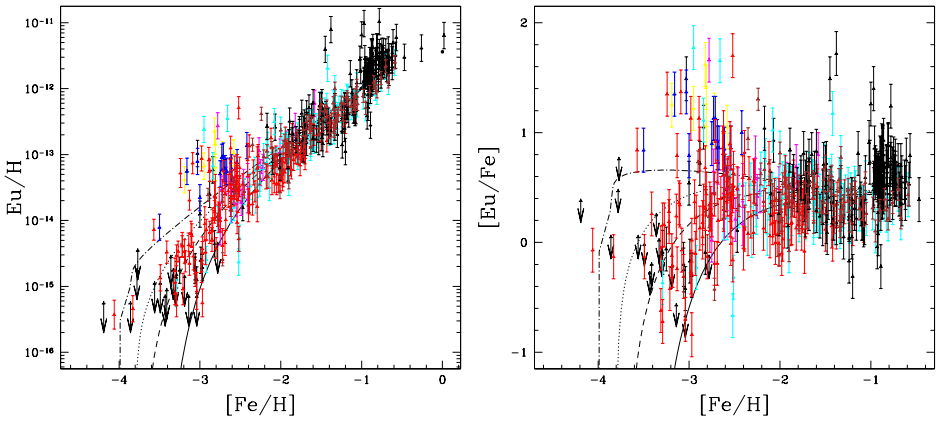


Figure 10. Cosmic evolution of Eu in the NSM scenario: effect of the coalescence timescale (SFR2 case). Same as Fig. 9 in SFR2 case.

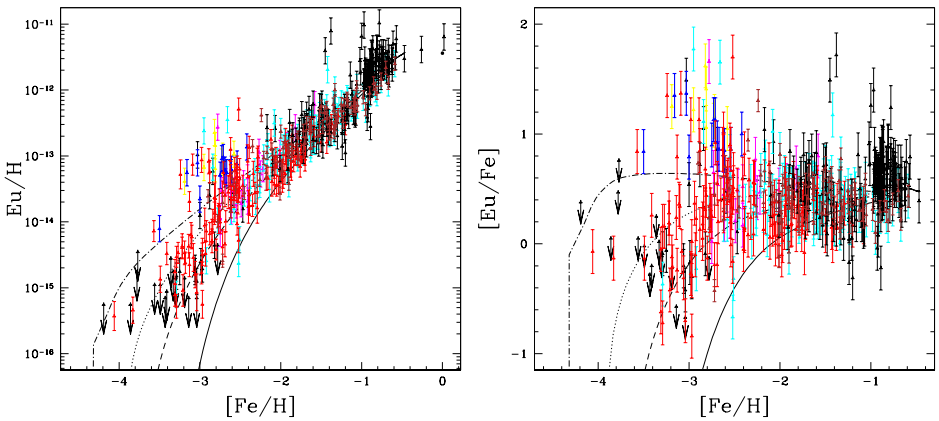


Figure 11. Cosmic evolution of Eu in the NSM scenario: effect of the coalescence timescale (SFR3 case). Same as Fig. 9 in SFR3 case.

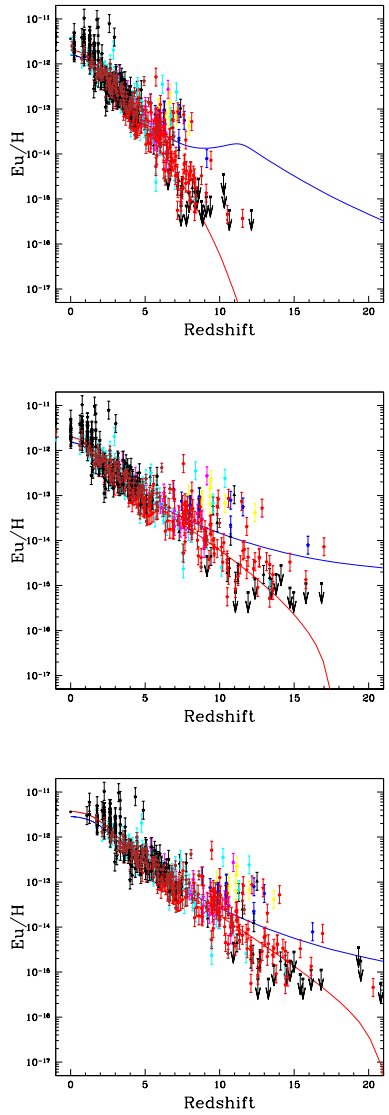


Figure 12. Cosmic evolution of Eu: comparison between the two possible astrophysical sites (2) Eu/H vs redshift. Evolution of Eu/H as a function of z either in the CCSN (blue lines) or in the NSM (red lines) scenario. The evolution is computed for the three SFR modes considered in the present study, SFR1 (upper panel), SFR2 (middle), SFR3 (lower panel). The three SFR modes are shown in different panels because the observations expressed in terms of [Fe/H] do not correspond to the same redshift z when different SFR are considered. The yields in the two scenarios are the same as in Fig. 7. In the NSM scenario, the binary fraction is $\alpha = 0.002$ and the coalescence timescale is 0.2 Gyr for the SFR1 mode, and 0.1 Gyr for the SFR2 and 0.05 Gyr for SFR3.

model, becomes almost equivalent to the predictions obtained with SFR2 and SFR3, as shown in Fig. 13.

4.4.2 Sensitivity to the early iron production

Our results depend on the adopted scenario for star formation in the Universe. This is why a detailed sensitivity study has been performed with different SFR stories, different stellar yields, with the

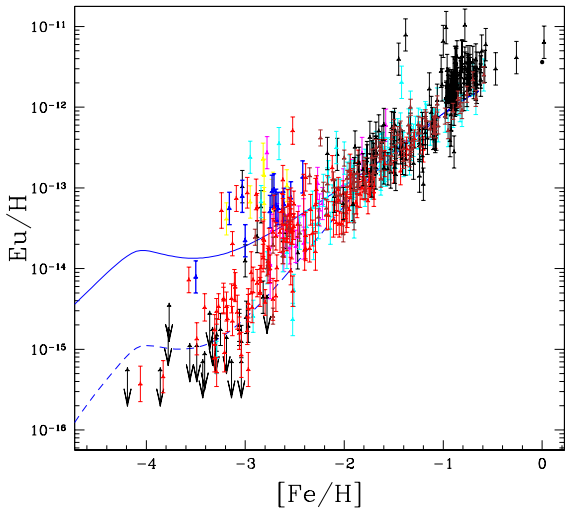


Figure 13. Cosmic evolution of Eu in the CCSN scenario: effect of the Eu yield (SFR1 case). Evolution of Eu/H as a function of [Fe/H] in the CCSN scenario for the SFR1 mode, assuming either the standard prescription for the Eu yield (solid line), i.e. 10^{-7} $M_{\odot}$ per supernova for massive stars at all metallicities, or a modified prescription (dashed line) where Eu is produced in supernovae only for massive stars with a metallicity $Z > 10^{-4} Z_{\odot}$.

aim of fitting the maximum of observational constraints, i.e. cosmological and local.

Recent studies published by other authors (Matteucci et al. 2014; Komiya et al. 2014) concluded that a merger time scale of the order of 1 - 10 Myr was necessary to reproduce the observed evolution of r elements with NS mergers alone. We find a different conclusion constraining the merger time scale to the range of 100 - 200 Myr. We made a careful analysis of the origin of this discrepancy. We show that the merger timescale depends strongly on the iron evolution which itself depends on the global astration rate and the choice of yields in supernovae or in hypernovae. Unfortunately, the CCSN production of Fe is poorly known. It depends essentially on the explosion energy and on the mass cut (fraction of the mass trapped in the remnant). Iron ejection is more important for higher energies of the explosion. Typically, we choose the SNII models by Woosley & Weaver (1995) ($E_{explod.} = 10^{51}$ ergs). At solar metallicity and for stars of 40 (20) $M_{\odot}$, they give an iron yield of 0.03 (0.02) $M_{\odot}$ respectively and 0.02 (0.1) $M_{\odot}$ respectively at Z = 0.001. On the other hand, hypernova models by Kobayashi et al. (2006) ($E_{explod.} = 10 - 30 \times 10^{51}$ ergs) correspond to 0.277 (0.035) $M_{\odot}$ of iron for the same stars at solar metallicity and 0.26 (0.08) $M_{\odot}$respectively at Z = 0.001. Indeed, hypernovae are much more energetical than the SNae. As seen in Fig. 14, a higher Fe early production constraints the merger time scale to be shorter. The studies by Matteucci et al. (2014); Komiya et al. (2014) assume stellar yields from Kobayashi et al. (2006) (hypernova case), whereas we assume the stellar yields from Woosley & Weaver (1995) (supernova case). We favor this assumption, since observations of the most metal-poor stars show a low iron abundance (Frebel and Norris 2015). It is worth noting that this result leading to merger timescales of the order of 100 - 200 Myr is in better agreement with our knowledge of the properties of the binary NS population (see Sect. 2.2.3).

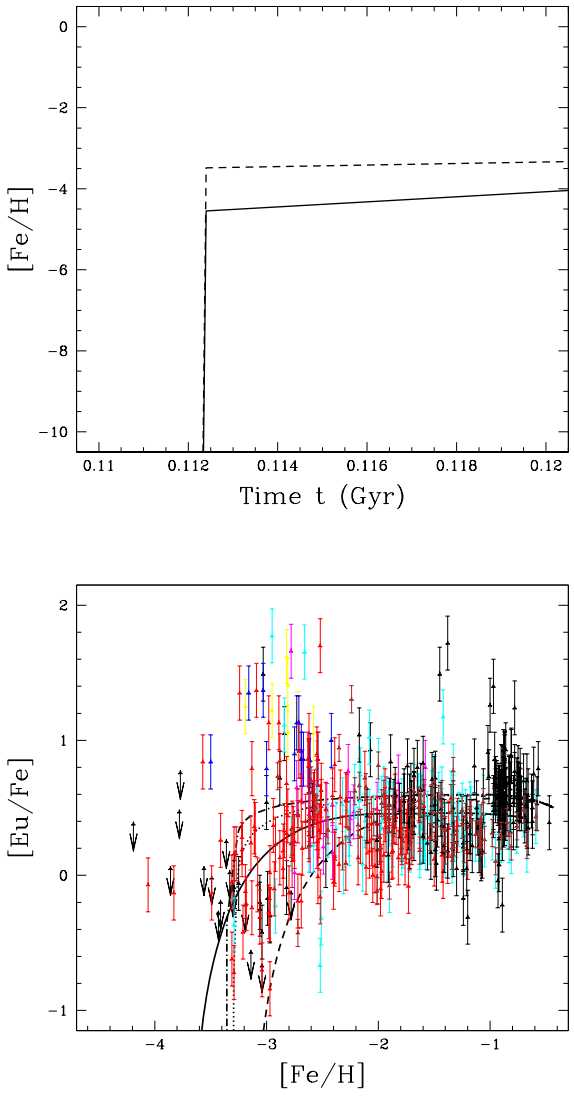


Figure 14. Cosmic evolution of Eu in the NSM scenario: sensitivity to the iron production and to the lower end of the IMF. Upper panel: evolution of [Fe/H] as a function of time in the SFR2 case, computed either with our standard prescription (solid line: Fe yields from Woosley & Weaver (1995), case B, and $M_{\rm inf}$ = 0.1 $M_\odot$ for the IMF), or with a modified prescription (dashed line: Fe yields from Kobayashi et al. (2006), hypernova case, and $M_{\rm inf}$ = 0.8 $M_\odot$ for the IMF) ; Lower panel: corresponding evolution of [Eu/Fe] as a function of [Fe/H]: our standard prescription for iron production (solid line) with a coalescence timescale of $\Delta t_{\rm NSM}$ = 0.1 Gyr is compared with the modified prescription for three values of the time delays, i.e. 0.1 Gyr (dashed line), 0.01 Gyr (dotted line), 0.001 Gyr, (dot-dash line).

As mentioned, the cosmic Fe enrichment plays a fundamental role in the interpretation of the chemical abundance evolution. To analyse the impact of this input on the determination of the NSM coalescence timescale, the Fe yield produced by massive stars has been varied in the SFR2 case. The standard yields of Woosley & Weaver (1995), more specifically their case B (for which low-metallicity high-mass stars do not produce iron), have been used. Note that (Heger & Woosley 2010) which follow the evolution and the explosion of zero-metallicity stars in the 10 – 100 $M_\odot$ range, obtain the same results regarding the production of iron. However, as said above, other studies find different conclusions; in particular, Kobayashi et al. (2006) predict higher iron yields than Woosley & Weaver (1995) for massive stars regardless of the metallicity. Fig. 14 illustrates the impact of Fe yields on the Eu evolution when considering the yields of Kobayashi et al. (2006). Note that we have also modified the lower end ($M_{\rm inf}$) of the IMF from 0.1 to 0.8 $M_\odot$ to increase the gas processing in stars and favor again the iron production.

With the yields of Kobayashi et al. (2006), iron at the very beginning of the evolution is seen to be synthesized earlier than in our standard model, leading to an overall abundance more than 10 times higher (Fig. 14, upper panel). We compare in Fig. 14 (lower panel) our standard SFR2 model with $\Delta t_{\rm NSM}$ = 0.1 Gyr (solid black line) with the results obtained with the yields of Kobayashi et al. (2006) and three different coalescence timescales, namely 0.1 Gyr (dashed line), 0.01 Gyr (dotted line) and 0.001 Gyr (dot-dash line). Consequently, a significant reduction of the coalescence timescale ($\Delta t_{\rm NSM}$ = 1 Myr) needs to be applied to compensate for the early increase in the Fe production in this context. It should be recalled that it is close to the scenario obtained by Matteucci et al. (2014) using the same Fe yields from Kobayashi et al. (2006) and an IMF with $M_{\rm inf}$ = 0.8 $M_\odot$. Clearly, the more iron is produced at early time, the shorter the predicted coalescence timescale required to explain the Eu abundance in the ultra-metal-poor stars.

4.4.3 *Time delay distribution and dispersion in data*

When fitting the observed early cosmic evolution of Eu in the NSM scenario, the coalescence timescale $\Delta t_{\rm NSM}$ is constrained to be short, typically in the range 50–200 Myr depending on the SFR (see § 4.3.1), as binary systems with longer timescales are not merging at large redshifts. As discussed in Sect. 2.2.3, such systems with a relatively low value of $\Delta t_{\rm NSM}$ represent a significant fraction of all the systems, but not all of them. In Fig. 15, we show the evolution of Eu using a broader, and more realistic, distribution of coalescence timescales. Based on the distribution plotted in Fig. 3, we assume 13% of the NSM in the 0–10 Myr range ($\Delta t_{\rm NSM}$ = 5 Myr), 10% in the 10–100 Myr range ($\Delta t_{\rm NSM}$ = 30 Myr), 15% in the 100–500 Myr range ($\Delta t_{\rm NSM}$ = 300 Myr), and 62% with a coalescence timescale above 500 Myr ($\Delta t_{\rm NSM}$ = 1 Gyr). The calculation is carried out for the SFR1 mode and we present the result for both α = 0.002 (solid line) and α = 0.004 (dotted line). When compared to Fig. 9, the early evolution is slightly modified due to the contribution of systems with even shorter coalescence timescales than in our reference case. As mergers are rare events with large Eu yields (compared to CCSN which are more frequent but produce less Eu), a large dispersion can be expected at low metallicity when only a small number of mergers affected the local environment. This could explain the observed dispersion shown in Fig. 7 and discussed in Sect. 4.1.

5 THE PREDICTED NSM RATE

Once the fraction α and the coalescence timescale $\Delta t_{\rm NSM}$ have been adjusted to reproduce the cosmic evolution of Eu, as described in the previous section, the cosmic evolution of the merger rate is determined as all free parameters entering in Eq. (4) are known. The result is plotted as a function of the redshift in Fig. 2 for the SFR1 and SFR3 modes, together with the CCSN rate and the NS and BH birth rates. The SFR evolution is shown for comparison.

Table 1. Predictions for the merger rate within the horizon of advanced Virgo/LIGO obtained with the constraint from the cosmic evolution of Eu using SFR1, SFR2, SFR3 models. For each SFR, the lower and higher values of the predicted rate correspond to the higher and lower limits on the yield of Eu in mergers, i.e. 2×10^{-4} $M_\odot$ and 7×10^{-5} $M_\odot$, respectively. The range of independent predictions compiled by Abadie et al. (2010) is given on the first line for comparison. Following Abadie et al. (2010), we adopt 200 Mpc (resp. 420 Mpc) for the size of the horizon for NS-NS (resp. NS-BH) mergers.

	NS-NS merger rate (yr^{-1})	NS-BH merger rate (yr^{-1})
Abadie et al. (2010)	40 (0.4–400)	10 (0.2–300)
SFR1	2.4 – 6.7	2.7 – 7.7
SFR2	2. – 5.7	2.3 – 6.87
SFR3	3.8 – 10.9	4.3 – 12.4

Table 2. Predictions for the kilonova rate for three different surveys: Palomar Transient Factory (PTF, limiting magnitude of 21 and area of 2700 deg^2, Law et al. 2010), Large Synoptic Survey Telescope (LSST, limiting magnitude of 24.5, area of 18000 deg^2, Abell et al . 2009) and Euclid (limiting magnitude of 24.5, area of 15000 deg^2, Laureijs et al. 2011) for SFR1, SFR2, SFR3 models. For each SFR, we consider either the most pessimistic case ('low') or the most optimistic case ('high') corresponding to the highest and lowest possibles values of the yield of Eu, as in Table 1. For each case, the range of predicted rates corresponds to the lowest and highest values of the peak luminosity of a kilonova (see text).

	Kilonova rate (yr^{-1})		
	PTF	LSST	Euclid
SFR1 low	0.0018 – 0.034	1.4 – 22.9	1.2 – 19.1
SFR1 high	0.005 – 0.096	4.1 – 65.4	3.3 – 54.5
SFR2 low	0.0014 – 0.028	1.2 – 20.1	1.0 – 16.7
SFR2 high	0.004 – 0.08	3.5 – 57.4	2.9 – 47.9
SFR3 low	0.003 – 0.054	2.3 – 36.4	1.9 – 30.3
SFR3 high	0.008 – 0.16	6.6 – 103.9	5.5 – 86.6

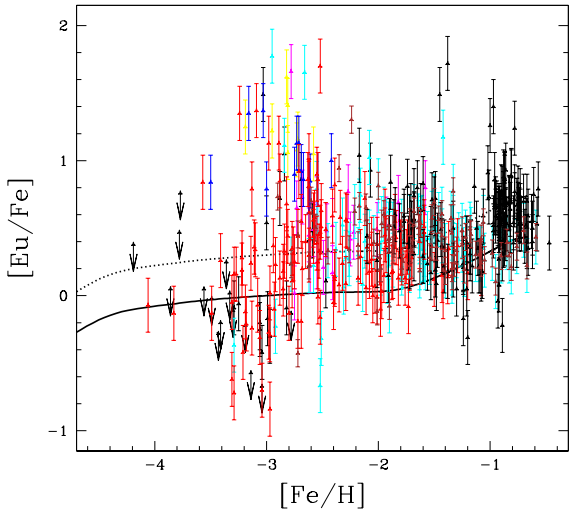


Figure 15. Eu evolution with a time delay distribution. Same as in Fig. 9 (SFR1 case) for a distribution of coalescence timescales corresponding to Fig. 3 (see text for more details). Solid and dotted curves correspond to two NSM fractions, of 0.002 and 0.004, respectively.

We also plot the local merger rate taken from the compilation by Abadie et al. (2010).

5.1 Merger rate in the horizon of gravitational wave detectors

On the basis of the cosmic evolution of the merger rate, it is possible to estimate the rate expected in the horizon of the gravitational wave detectors advanced Virgo and ad LIGO and to compare those rates with independent predictions, as compiled by Abadie et al. (2010). The result is plotted in Fig. 16 for the SFR1 scenario. When considering the production of Eu in the NSM scenario, both parameters, the Eu yield and the fraction of binary mergers α, are degenerate when adjusted on the cosmic evolution of Eu. This is not the case for the calculation of the event rates. Therefore, we present in Fig. 16 the results for two sets of parameters: either our standard Eu yield of 7×10^{-5} $M_\odot$ and a binary fraction $\alpha = 0.002$ (solid lines), or a larger Eu yield of 2×10^{-4} $M_\odot$ (as found in NSM simulations, see Sect. 4.2.2) and a lower binary fraction $\alpha = 0.0007$ (dashed lines), both leading to exactly the same cosmic evolution of Eu. The predicted rates are given in Table 1 for the two extreme sets of parameters.

Interestingly, the integrated merger rate in the horizon of gravitational wave detectors obtained in the present study using our standard value for the Eu yield from NSM (7×10^{-5} $M_\odot$) is close to the central value of the predictions compiled by Abadie et al. (2010). In contrast the upper value of the Eu yield tends to disfavor the upper half of the predicted range given by Abadie et al. (2010), as clearly illustrated in Fig. 16.

5.2 Kilonova rate

As discussed in the introduction, NS-NS/BH mergers can potentially have two main types of electromagnetic counterparts, short GRBs and kilonovae. Short GRBs are associated to the pro-

[htb!]

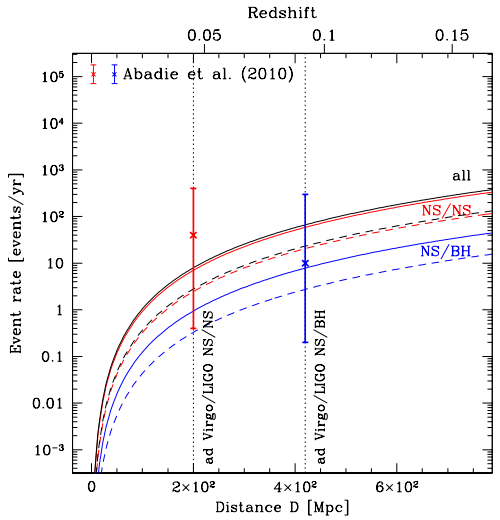


Figure 16. The integrated merger rate (NS-NS, red line, NS-BH, blue line, and total, black line) as a function of the distance (lower axis) and the redshift (upper axis). Two vertical lines indicate the size of the horizon of the gravitational wave detectors advanced Virgo/LIGO. For comparison, the central value and range of the predicted rates within this horizon compiled by Abadie et al. (2010) is also indicated for both types of mergers. The calculation corresponds to the SFR1 mode with the standard prescription (solid line: Eu yield of 7×10^{-5} $M_\odot$ and binary fraction $\alpha = 0.002$) and with a modified prescription (dashed line: 2×10^{-4} $M_\odot$ and binary fraction $\alpha = 0.0007$), both leading to exactly the same cosmic evolution of Eu plotted in Fig. 7.

[htb!]

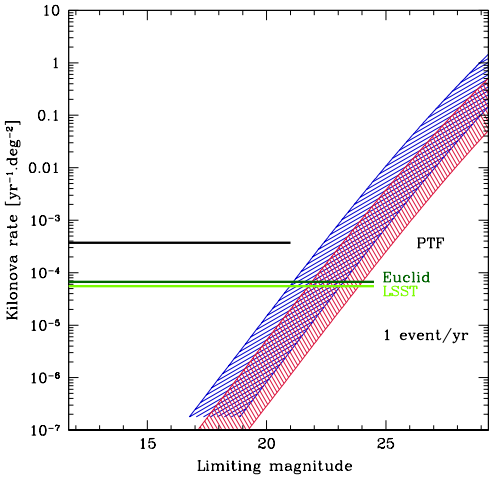


Figure 17. The integrated kilonova rate per deg^2 as a function of the limiting magnitude for the two same cases as in Fig. 16, i.e. SFR1 with the standard prescription (blue) or the modified prescription (red) for the Eu yield. The width of the shaded area in each case takes into account the theoretical uncertainties on the peak luminosity of the kilonova (see Eq. (12)). For comparison, horizontal yellow and green lines indicate the limit of 1 event per year for three surveys (PTF, LSST and Euclid, see Sect. 5.2 and Table 2 for the limiting magnitude and area of each survey).

duction of an ultra-relativistic outflow along the polar axis of the post-merger BH-torus system, with large uncertainties on the beaming angle of the jet. Therefore, the prediction of the short GRB rate from the merger rate requires a specific treatment (see e.g. Guetta & Piran 2006; Wanderman & Piran 2015; Fryer et al. 2012), which we do not include in the present study. On the other hand, kilonovae are associated with a quasi-isotropic non-relativistic ejection that should be present in all systems. The luminosity of the kilonovae is powered by the radioactive decay of freshly synthesized elements and is consequently directly related to the nucleosynthesis of r-process nuclei. Note that NS/NS mergers are better sources of electromagnetic emission, as the ejected mass is very low in a noticeable fraction of NS/BH mergers (see Fig. 7 in Belczynski et al. (2008b)). As NS/BH mergers are about one order of magnitude less frequent than NS/NS mergers (see, Fig. 16), this does not affect our results.

Therefore, the detection of a kilonova would represent a major step to probe the contribution of NS-NS/BH mergers to the synthesis of heavy elements in the Universe (see also Metzger et al. 2015). There is only one or two tentative detections to date. The first candidate is in association with the short GRB 130603B (Berger et al. 2013; Tanvir et al. 2013). However, this observation is not detailed enough (only a single photometric measurement) to prove firmly its kilonova nature. The second candidate is associated to GRB 060614, whose short or long nature is ambiguous, but is also based on a photometric near-infrared bump only (Yang et al. 2015). More detections, with a photometric and spectroscopic follow-up, will be required to progress further. The peak of the kilonova is expected in the near-infrared range a few days after the merger (it may be bluer in the case of NS/BH mergers, a et al. 2014). The long-term evolution of the ejecta, which is decelerated by the ambient medium, also leads to radio emission over weeks. This signal is not considered here though it may also become detectable by future radio surveys (Nakar & Piran 2011; Piran et al. 2013).

Our model allows to constrain the expected rate of kilonovae for a given large survey as a function of the limit magnitude in the optical/near-infrared range. Following Metzger et al. (2010), the peak luminosity scales as

$$L_{\rm KN,peak} \simeq 5 \times 10^{40}\ {\rm erg/s} \left(\frac{f}{10^{-6}}\right)\left(\frac{v}{0.1c}\right)^{1/2}\left(\frac{M_{\rm ej}}{10^{-2}\,M_\odot}\right)^{1/2}, \qquad (12)$$

where v and $M_{\rm ej}$ are the velocity and mass of the ejecta respectively and f is the heating efficiency (Arnett 1982; Li & Paczyński 1998; Metzger et al. 2010). Compared to Metzger et al. (2010), the normalization in Eq. 12 has been corrected for a more realistic opacity of the r-process elements, which is expected to be $\sim 10^2$ times larger compared to the opacity of iron group elements considered in previous studies (Kasen et al. 2013) (see also Kasen et al. 2015). Using the extreme values obtained in the systematic study of the dynamics of the ejecta carried out by Bauswein et al. (2013), this leads to $L_{\rm KN,peak} \simeq (2.0 - 14) \times 10^{40}$ erg/s (see also Grossman et al. 2014).

Assuming that all kilonovae have similar peak luminosities $L_{\rm KN,peak}$, we can deduce from the merger rate the number of kilonovae per year above a given flux. This leads to the results plotted in Fig. 17, where the rate of kilonovae per year and per square degree is plotted as a function of the limiting magnitude of a given survey, in the SFR1 case with the two same sets of parameters (Eu yield, compact binary fraction α) as in Fig. 16. The width of

the shaded area takes into account the range of $L_{\rm KN,peak}$ discussed above. Horizontal lines indicate the limit above which at least one event per year is expected for different surveys, taking into account their magnitude limit and their field of view. The results are listed in Table 2 for each SFR and for the two extreme values of the yield of Eu. It appears that the current Palomar Transient Factory (PTF) survey (limiting magnitude of 21 and area of 2700 deg^2) fails to detect kilonovae, whereas the predictions are more optimistic for future surveys like the Large Synoptic Survey Telescope (LSST, limiting magnitude of 24.5, area of 18000 deg^2) and mostly Euclid (limiting magnitude of 24.5, area of view of 15000 deg^2) with a well adapted spectral range, for which typically $\sim 2-100$ events per year can be expected.

6 CONCLUSIONS

We have computed the predicted evolution of the cosmic rates of CCSN and NSM for three possible history of the SFR density, which are representative of the current uncertainties at high redshift and reproduce important observational constraints such as the cosmic evolution of iron or the Thomson optical depth to CMB. We have deduced the corresponding expected evolution of Eu, a typical r-process elements, considering that the astrophysical sites for the r-process are either CCSN or NSM. In the latter case, the comparison to observations is used to constraint two free parameters, the binary fraction of compact objects and the typical coalescence timescale in NS binary systems. We obtain the following results:

(i) The r-process evolution using the NSM scenario as the main astrophysical site is in good agreement with observations, assuming that the early evolution is dominated by mergers of binary systems with a coalescence timescale of the order of $\Delta t_{\rm NSM} \sim 100$ Myr. Such mergers represent a significant fraction of all mergers according to recent estimations obtained with detailed population synthesis codes;
(ii) In this merger scenario, the explosive events responsible for the production of r-process elements are more rare than in the supernova scenario, but each event yields more Eu. Therefore, a larger scattering in the r-process abundance is expected in metal-poor stars enriched by mergers. We present calculations of the early evolution of Eu obtained when summing up contributions of mergers with a broad range of coalescence timescales according to predictions of population synthesis models and we find a reasonable agreement with the level of scatter observed. At high metallicities, the cumulative effect leads to a low sensitivity with respect to the coalescence timescale;
(iii) The precise constraint on the dominant coalescence timescale relevant for the early evolution of Eu depends on the adopted SFR at high redshift, for which we have tested three scenarios representative of the current uncertainties, and on the iron yields of stars at low metallicity, for which we have compared two theoretical predictions made by either Woosley & Weaver (1995) or Kobayashi et al. (2006). The conclusion is that shorter coalescence timescales are favored by scenarios for which the production of iron at early times is more intense, i.e. for larger SFR at high redshift and larger iron yields coming from CCSN. In the standard conditions, we constrain the coalescence timescale $\Delta t_{\rm NSM}$ to be in the range of 50-200 Myr;
(iv) In the merger scenario which is favored by observations at low metallicity, two additional parameters are degenerate: the fraction α of NS in a binary system with another NS or a BH and the yield of Eu per merger. This second parameter is constrained to be in the range 7×10^{-5}–$2\times10^{-4}\ M_\odot$ per merger in the most recent nucleosynthesis calculations. Adopting these two values leads to an upper and a lower limit on α ($0.002-0.0007$) which constrain the merger rate as a function of the redshift in the Universe;
(v) We use the previous calculation to predict the expected rate of mergers within the horizon of gravitational wave detectors. We find that the predicted rate as constrained by the cosmic evolution of Eu falls well within the range of predictions by other independent methods compiled by Abadie et al. (2010) but clearly favors the mid or lower values, and not the most optimistic predictions. We predict typically 2 to 10 NS-NS mergers per year and an equivalent number of NS-BH mergers per year;
(vi) Considering the most recent estimates of the opacity of r-process elements, we also predicted the rate of kilonovae in current and future optical/near-infrared large surveys. Our results are compatible with the lack of kilonova detections by PTF and are optimistic for the future LSST and Euclid projects, though with a large uncertainty: from 1 kilonova per year in the most pessimistic case to 100 events per year in the most optimistic case.

Our results can be improved in the future in several ways. Successful r-process in CCSN with well-defined Eu yields, including a possible dependence with metallicity, would be very useful to definitively check the consistency of this scenario with observations. A better determination of the SFR at large redshift and a convergence of theoretical predictions for iron yields in primordial CCSN would also strongly reduce the uncertainties on the parameters of the model in the merger scenario. In addition, more measurements of the abundance of r-process elements in stars at even lower metallicity ([Fe/H] < -3.5) would also allow to better constrain the model parameters. Finally, the predictions for the kilonova detection rate in future surveys could be improved by taking into account the correction for the spectral range of the instruments. Additional predictions for the rates of other transients associated with mergers, i.e. short gamma-ray bursts and radio flares, could also be deduced from the predicted merger rate to provide new diagnostics in the future.

ACKNOWLEDGEMENTS

EV thanks warmly Keith Olive, Jean-Pierre Lasota and Tsvi Piran for constant and fruitful discussions. The authors thank specifically Gilles Esposito-Farèse for his help on the physics of mergers. EV and FD acknowledge the French Program for High Energy astrophysics (PNHE) for financial support. K.B. is sponsored by the NCN grant Sonata Bis2 (DEC - 2012/07/ST9/01360) and by the polish Science Foundation ”Master” subsidy. This work is made in the ILP LABEX (under reference ANR-10-LABX-63) supported by French state funds managed by the ANR within the Investissements d’Avenir programme under reference ANR-11-IDEX-0004-02. SG is FRS-FNRS research associate.

REFERENCES

Aasi, J., et al., 2014a, Phys. Rev. D, 89, 12003
Aasi, J., et al., 2014b, Phys. Rev. D, 89, 12004
Aasi, J., et al., 2014c, Phys. Rev. D, 90, 2010
Abadie, J. et al. 2010, Classical and Quantum Gravity, 27, 173001
Abell, P. A., Allison, J., et al., LSST Science Collaboration 2009, arXiv:0912.0201
An, D., Beers, T.C., Johnson, J.A. et al.2013, ApJ, 763, 65

Argast, J. et al. 2004, A&A, 416, 997
Arnett, W. D. 1982, ApJ, 253, 785
Arnould, M., Goriely, S., & Takahashi, K. 2007, Phys. Rep., 450, 97
Asplund, M., Grevesse, N. Sauval, A.J., Scott, P. 2009, Ann. Rev. Astron. Astroph., 47, 481
Barklem, P. S, et al. 2005, A&A, 439, 129
Bauswein, A., Goriely, S. & Janka, H.T 2013, ApJ, 773, 78
Bauswein, A., Ardevol Pulpillo, R., Janka, H.T, & Goriely, S. 2014, ApJ, 795, L9
Behroozi, P. S., Wechsler, R. H., & Conroy, C. 2013, ApJ, 770, 57
Behroozi, P. S. & Silk, J. 2015, ApJ, 799, 32, arXiv 1404.5299
Belczynski, K. et al. 2002, ApJ, 572, 407
Belczynski, K., Taam, R. E., Kalogera, V., Rasio, F. A., & Bulik, T. 2007, ApJ, 662, 504
Belczynski, K. et al. 2008a, ApJ, Suppl. 174, 223
Belczynski, K. et al. 2008b, ApJ, 682, 474
Belczynski, K. et al., 2014, ApJ, 789, 120
Berger, E., Fong, W. & Chornock, R. 2013, ApJ, 774, L23
Berger, E. 2014, Ann. Rev. Astron. Astroph., 52, 43
Bošnjak, Ž., & Daigne, F. 2014, A&A, 568, AA45
Bouwens, R. J., Illingworth, G. D., Franx, M., & Ford, H. 2007, ApJ, 670, 928
Bouwens, R. J., Illingworth, G. D., Franx, M., & Ford, H. 2008, ApJ, 686, 230
Bouwens, R. J., Illingworth, G. D., Oesch, P. A., et al. 2011, ApJ, 737, 90
Bouwens, et al. 2014, ApJ, 795, 126
Cescutti, G. & Chiappini, C. 2014, A&A 565, A51
Cohen, J. G., Huang, W. 2009 ApJ, 701, 1053
Eichler, D., Livio, M., Piran, T., & Schramm, D. N. 1989, Nat, 340, 126
Daigne, F., Olive, K. A., Vangioni-Flam, E., Silk, J., & Audouze, J. 2004, ApJ, 617, 693
Daigne, F., Olive, K. A., Silk, J., Stoehr, F., & Vangioni, E. 2006, ApJ, 647, 773
Dominik, M., Belczynski, K., Fryer, C., Holz, D.E., Berti, E., Bulik, T., Mandel, I. & O'Shaughnessy, R. 2012, ApJ, 759, 52
Dominik, M. et al. 2013, ApJ, 779, 72
Dominik, M. et al. 2015, ApJ, 806, 263, arXiv 1405.7016
Dvorkin, I., Silk, J., Vangioni, E., petitjean P. & Olive, K. 2015, in press MNRASL, 452L, 36, arXiv 1506.06761
Fischer, T., Whitehouse, S. C., Mezzacappa, A., Thielemann, F.-K., & Liebendörfer, M. 2010, A&A, 517, A80
François, P. et al. 2007, A&A, 476, 935
Frebel, A. & Norris, J.E. 2015, arXiv:1501.06921
Freiburghaus, C., Rosswog, S., Thielemann, F.-K. 1999, ApJ, 525, L121
Fryer, C.L., Belczynski, K., et al. 2012, ApJ, 749, 91
Fryer, C.L., Belczynski, K., et al. 2015, arXiv:1504.07605
Geisler, D., Smith, V. V., Wallerstein, G., Gonzalez, G., Charbonnel, C. 2005 AJ, 129,1428
Goriely, S., Demetriou, P., Janka, H.-T. & Pearson, J.M. 2005, NPhysA, 758, 587c
Goriely, S., Bauswein, A. & Janka, H.S. 2011, ApJL, 738, L32
Goriely, S., Sida, J.-L., Lemaître, J.-F., Panebianco, S., Dubray, N., Hilaire, S., Bauswein, A. & Janka, H.-T 2013, Phys. Rev. Lett., 111, 242502
Greif, T.H. & Bromm V. 2006, MNRAS, 373, 128
Grossman, D., Korobkin, O., Rosswog, S., & Piran, T. 2014, MNRAS, 439, 757
Guetta, D. & Piran, T. 2006, A&A 453, 823
Guiriec, S., Briggs, M. S., Connaugthon, V., et al. 2010, ApJ, 725, 225
Hansen, T. et al. 2014, ApJ, 787, 162, arXiv 1405.5846
Hartwick, F. D. A. 1976, ApJ 209, 418
Heger, A. & Woosley, S. E. 2010, ApJ, 724, 341
Hinshaw, G., Larson, D., Komatsu, E., et al. 2013, ApJS, 208, 19
Honda, S. et al.. 2004, ApJ, 607, 474
Hüdepohl, L., Müller, B., Janka H.-T., Marek., A., & Raffelt, G.G. 2010, Phys. Rev. Lett., 104, 251101
Hughes, S. A. 2009, Ann. Rev. Astron. Astroph., 47, 107
Hulse, R. A., & Taylor, J. H. 1975, ApJL, 195, L51
Janka, H.-T., Eberl, T., Ruffert, M., & Fryer, C.L. 1999, ApJL, 527, L39
Janka, H.-T. 2012, Ann. Rev. Nuc. Part. Science, 62, 407
Jenkins, A., Frenk, C. S., White, S. D. M., Colberg, J. M., Cole, S., Evrard, A. E., Couchman, H. M. P., & Yoshida, N. 2001, MNRAS, 321, 372
Just, O. et al. 2015, MNRAS, 448, 541, arXiv1406.2687
Kalogera, V., Narayan, R., Spergel, D.D. & Taylor, J.H. 2001, ApJ, 556, 340
Kalogera, V. et al. 2004, ApJ, 614, L137 and 601, L179
Kasen, D., Badnell, N.R. & Barnes, J. 2013, ApJ, 774, 25
Kasen, D., Fernandez, R. & Metzger, B.D. 2015, MNRAS, 450, 1777, arXiv 1411.3726
Kim C. , Kalogera, V. & Lorimer, D.R. 2003, ApJ, 584, 985
Kistler, M.D. et al.. 2013, arXiv1305.1630
Kobayashi, C. et al.. 2006, ApJ, 653, 1145
Komiya, Y. et al. 2014, ApJ, 783, 132
Korobkin, O., Rosswog, S., Arcones, A. & Winteler C. 2012, MNRAS, 426, 1940
Lattimer, J.M. & Schramm, D.N. 1974, ApJ,192, L145
Lattimer, J.M., Mackie, F., Ravenhall, D.G., & Schramm, D.N. 1977, ApJ, 213, 225
Laureijs, R., Amiaux, J., Arduini, S., et al. 2011, arXiv:1110.3193
Law, N. M., Dekany, R. G., Rahmer, G., et al. 2010, Proc. SPIE, 7735, 77353M
Li, L.-X. & Paczyński, B. 1998, ApJL, 507, L59
Letarte, B., Hill, V., Tolstoy, E., Jablonka, P., Shetrone, M., et al.. 2010, A&A, 523, A17
LIGO Scientific Collaboration, & Virgo Collaboration, 2011, Advanced LIGO anticipated sensitivity curves, *https://dcc.ligo.org/cgi-bin/DocDB/ShowDocument?docid*
Lodders, K. 2003, ApJ, 591, 1220
Lorimer, D.R., 2005, JJMPA, 20, 7035
Lorimer, D. R. 2008, Living Reviews in Relativity, 11, 8
McMillan, P. J. 2011, MNRAS, 414, 2446
McWilliam, A., Wallerstein, G., Mottini, M. 2013 ApJ, 778,149
Maeder A. & Meynet G., 1989, A&A, 210, 155
Mattila S., Dahlen T., Efstathiou A., et al., 2012, ApJ, 756, 111
Matteucci, F. et al. 2014, MNRAS, 438, 2177
Mennekens, N. & Vanbeveren, D. 2014, A&A, 564, A134
Metzger, B.D., Martinez-Pinedo, G., Darbha, S., et al. 2010, MNRAS, 406, 2650
Metzger, B.D., Bauswein, A., Goriely, S. & Kasen, D., 2015, MNRAS, 446, 1120
Meyer, B.S. 1989, ApJ, 343, 254
Mochkovitch, R., Hernanz, M., Isern, J., & Martin, X. 1993, Nat, 361, 236
Nakar, E. 2007, PhysRep, 442, 166
Nakar, E., & Piran, T. 2011, Nat, 478, 82
Narayan, R., Piran, T., & Shemi, A. 1991, ApJL, 379, L17
Narayan, R., Paczynski, B., & Piran, T. 1992, ApJL, 395, L83

Ryan, S. G., & Norris, J. E. 1991, AJ, 101, 1865
Oechslin, R., Janka, H.-T., & Marek, A. 2007, A&A, 467, 395
Oesch, P. A., Bouwens, R. J., Illingworth, G. D., et al. 2012, ApJ, 759, 135
Oesch, P. A., Bouwens, R. J., Illingworth, G. D., et al. 2013, ApJ, 773, 75
Oesch, P. A., Bouwens, R. J., Illingworth, G. D., et al. 2014, ApJ, 786, 108
O'Shaughnessy, R., Kim, C., Kalogera, V., & Belczynski, K. 2008, ApJ, 672, 479
Paczynski, B. 1986, ApJL, 308, L43
Peters, P. C., & Mathews, J. 1963, Physical Review, 131, 435
Phinney, E. S. 1991, ApJL, 380, L17
Piran, T., Nakar, E., & Rosswog, S. 2013, MNRAS, 430, 2121
Planck Collaboration, Ade, P. A. R., Aghanim, N., et al. 2014, A&A 566, 54, arXiv:1311.1657
Planck Collaboration, Ade, P. A. R., Aghanim, N., et al. 2015, arXiv:1502.01589
Postnov, K. A., & Yungelson, L. R. 2014, Living Rev. Rel., 17, 3
Press, W. H., & Schechter, P. 1974, ApJ, 187, 425
Rafelski, J., Christlieb, N. & Zhao, G. 2012, A&A, 537, 118
Ramirez-Ruiz, E. et al.. 2015, ApJL, 802, L22, arXiv: 1410.3467
Ren, M., et al. 2012, ApJ, 755, 89
Rezzolla, L., Giacomazzo, B., Baiotti, L., et al. 2011, ApJL, 732, L6
Roberts, L.F., Kasen, D., Lee, W.H., & Ramirez-Ruiz, E. 2011, ApJ, 736, L21
Roederer, I.U. et al. 2010, ApJ, 724, 975
Roederer, I.U. 2011, ApJ, 732, L17
Roederer, I.U. et al. 2012, ApJS, 203, 27
Roederer, I.U. et al. 2014, ApJ, 784, 158
Roederer, I.U. et al. 2014, AJ, 147, 136
Roederer, I.U. et al. 2014, MNRAS, 445, 2970
Rollinde, E., Vangioni, E., Maurin, D., Olive, K. A., Daigne, F., Silk, J., & Vincent, F. H. 2009, MNRAS, 398, 1782
Rosswog, S., Liebendörfer, M., Thielemann, F.-K., Davies, M.B. & Piran, T. 1999, A&A, 341, 499
Rosswog, S., Speith, R., & Wynn, G.A. 2004, MNRAS, 351, 1121
Rosswog, S., Korobkin, O., Arcones, A., Thielemann, F.-K., & Piran, T. 2014, MNRAS, 439, 744
Sana, H. de Mink, S.E., de Koter, A., et al., 2012, Science, 337, 444
Schaerer, D. 2002, A&A, 382, 28
Shen, S., Cooke, R., Ramirez-Ruiz, E., Madau, P., Mayer, L., & Guedes, J. 2014, arXiv:1407.3796
Shetrone, M., Côté, P., Stetson, P. B. 2001, PASP, 113, 1122
Shetrone, M., Venn, K. A., Tolstoy, E., Primas, F., Hill, V., Kaufer, A. 2003, AJ125, 684
Sheth, R. K., & Tormen, G. 1999, MNRAS, 308, 119
Simmerer, J., et al.2004, ApJ, 617, 1091
Sneden, C., Cowan, J.J., & Gallino, R. 2008, ARA&A, 46, 241
Springel, V. & Hernquist L., 2003, MNRAS, 339, 312
Starkenburg, E.; Hill, V.; Tolstoy, E.; Franois, P.; Irwin, M. J.; Boschman, L.; Venn, K. A.; de Boer, T. J. L.; Lemasle, B.; Jablonka, P.; Battaglia, G.; Groot, P.; Kaper, L. 2013 A&A 549, 88
Suda, T., et al., 2008, PASPJ, 60, 1159
Suda, T., et al., 2011, MNRAS, 412, 843
Tanaka, M., Hotokezaka, K., Kyutoku, K., et al. 2014, ApJ, 780, 31
Tanvir, N.R. et al. 2013, Nature, 500, 547
Trenti, M., Perna, R., & Tacchella, S. 2013, ApJL, 773, L22
Tsujimoto, T. & Shigeyama, T. 2014, A&A, 565, L5
Tsujimoto, T. & Shigeyama, T. 2014, ApJL, 795, L518
Tsuruta, S. & Cameron, A.G.W. 1965, Can. J. Phys., 43, 2056
Tutukov, A. V., & Yungelson, L. R. 1993, Astronomy Reports, 37, 411
van de Voort, F., Quataert, E., Hopkins, P. F., Keres, D., & Faucher-Giguere, C.-A. 2015, MNRAS, 447, 140, arXiv:1407.7039
Vangioni, E. et al. 2014, MNRAS, 447, 2575, arXiv:1409.2462
Vink, J.S., Muijres, L.E., Anthonisse, B. et al., 2011, A&A, 531, 132
Vink, J.S. & Grafener, G., 2012, ApJL, 536, L10
Virgo Collaboration. 2009, Advanced Virgo Baseline Design, Virgo Technical Report VIR-0027A-09, *https://tds.ego-gw.it/itf/tds*
Voss, R., & Tauris, T. M. 2003, MNRAS, 342, 1169
Wanajo, S., Janka, H.-Th., & Müller, B., 2011, ApJL, 726, L15
Wanajo et al. 2014, ApJL, 789, L39
Wanderman, D., & Piran, T. 2015, MNRAS, 448, 3026, arXiv:1405.5878
Wang, F. Y. 2013, A&A, 556, A90
Weisberg, J.M., Nice, D.J. & Taylor, J.H., 2010, ApJ, 722, 1030
Woosley, S. E. & Weaver, T. A. 1995, ApJS, 101, 181
Worley, S. et al. 2013, A&A, 553, 47
Wyithe, J. S. B., & Loeb, A. 2003, ApJL, 588, L69
Yang, B., Jin, Z.-P., Li, X., et al. 2015, Nature Communications, 6, 7323